Development of Analytical Model for Bonding of CFRP Rod in Concrete Subjected to Cyclic Loads

Arash Azarkerdar [1] and Farzad Hejazi [2,*]

1 Department of Civil Engineering, University Putra Malaysia, Serdang 43400, Malaysia; arash.azarkerdar@gmail.com
2 Faculty of Environment and Technology, The University of the West England, Bristol BS16 1QY, UK
* Correspondence: farzad@fhejazi.com

Abstract: Recent material science advances have resulted in the use of High-Performance Concrete (HPC) and Ultra-High-Performance Concrete (UHPC) in superstructures, which were chosen for their superior strength. However, under cyclic loads, these materials frequently show fatigue. Carbon-Fibre-Reinforced Polymer (CFRP) rods are replacing steel rebars due to their corrosion resistance and excellent strength-to-weight ratio and are thus gaining popularity in both infrastructural and superstructural design. However, due to a lack of understanding of their bond mechanics, modelling the interaction between CFRP rods and these advanced concretes in finite element simulations remains complex, particularly under cyclic loading. The bond behaviour of CFRP rods and both standard Grade 40 concrete and Ultra High-Performance Fibre-Reinforced Concrete (UHPFRC) under cyclic stresses is investigated in this work. A finite element model of connected concrete cube samples was built and analysed under cyclic stress, combining these concretes with CFRP rods. Furthermore, these samples were subjected to dynamic actuation testing to develop a traction-based constitutive model for the CFRP–concrete interface. In finite element models, an interface element devised for this study effectively approximated the binding, matching experimental data. The new analytical interface element improved simulation precision by 19% in displacement and 49% in pull-out force, resulting in a significant improvement in predicting the performance of the CFRP–UHPFRC bond under cyclic loading. The improved performance of the CFRP–UHPFRC bond under cyclic loading is attributed to the optimised interface model that enhances the bond integrity between CFRP rods and concrete.

Keywords: CFRP–UHPFRC interface; FEA of CFRP embedded in concrete; cyclic bond strength enhancement; cyclic load response modelling; interface element development for bond simulation; durability characteristics under cyclic loading

1. Introduction

Concrete, which has been fundamentally used in the realm of construction, owes its enhanced properties to the advent of reinforced concrete. This significant advancement, credited to Joseph Monier in 1849, marries the flexural strength of metal with concrete's inherent compressive resilience, enabling structures to withstand formidable loads [1].

Superstructures—encompassing bridges, transportation corridors, and skyscrapers—are often plagued by fatigue failures arising from the relentless imposition of cyclic loads. Bridges epitomise vulnerability in this context, with cyclic loading precipitating fatigue failure, environmental degradation, and thus potential collapse. The material sciences field has witnessed considerable strides, particularly with the advent of High-Performance Concrete (HPC) and Ultra-High-Performance Concrete (UHPC), which have found favour in modern construction practices [2]. Investigations by Scott Muzenski and Benjamin Graybeal into UHPC overlays for bridge decks have underscored the material's exceptionally low permeability, directly contributing to an extension of the structure's service life. The

duo undertook both cyclic and static loading tests on traditional concrete substrates augmented by UHPC overlays. Their findings elucidate the reinforcement potential of UHPC overlays in sustaining bridge deck integrity, with a pressing emphasis on the precision of joint detailing [3]. Parallel research efforts by You et al. have explored the potential of using recycled macrofibres from discarded Glass-Fibre-Reinforced Polymer (GFRP) composites to reinforce UHPC, aiming to mitigate costs and environmental repercussions. Despite observing a reduction in workability and compressive strength—up to 21.8%—the studies revealed significant gains in flexural strength and toughness, suggesting a sustainable and economically viable path forward for the UHPC domain [4]. In a similar vein, Ali A. Semendary and Dagmar Svecova's engagement with numerical simulations via finite element modelling elucidated the bonding dynamics at UHPC interfaces. Their research unravelled strategies to augment the bonding strength in precast UHPC elements, evidenced by alignment between their model outcomes and empirical data [5]. Now, modern imbroglios demand that the quest for reliability, efficiency, and sustainable innovation in construction never ceases. One such innovation has been the integration of Fibre-Reinforced Polymer (FRP) sheets, which has proven pivotal for the refurbishment and repair of enfeebled structures. The substantive contribution of FRPs in extending the service life of existing buildings through novel applications—from cloaking cracks and improving thermal insulation to bolstering the shear and flexural integrity of concrete elements—cannot be overstated. However, the tale of FRP extends beyond mere structural rehabilitation; it includes preventive applications in otherwise robust structures to enhance their resilience against future uncertainties [6]. The advent of Carbon-Fibre-Reinforced Polymer (CFRP) marked a milestone in this narrative, touted for its superior corrosion resistance to traditional steel reinforcements. The implementation of CFRP as a substitute for steel bars has been largely driven by its remarkable durability in hostile environmental conditions. The pursuit of understanding the full potential of CFRP has spanned various methodologies of application, including the Embedded Through Section (ETS), which has been proven to enhance shear capacity commendably compared to its counterparts—Externally Bonded (EB) and Near Surface Method (NSM). These methods, EB and NSM, themselves have shown shear capacity increases of 23% and 31%, respectively. However, these innovations also delineated the challenges of bonding CFRP with UHPFRC, notably the reductions in bond strength observed when increasing the embedment length, a phenomenon exacerbated by the nature of the composite materials [7,8]. The intricacies of CFRP's bonding with concrete also manifest in the load–slip relationship, a paramount factor in structure longevity. For instance, the pull-out behaviour of CFRP and AFRP reinforced rods is governed by distinct load–slip profiles. The AFRP rod exhibits a linear relationship until a certain slip threshold, after which yield occurs. Contrastingly, CFRP demonstrates a non-linear frequency under loading with higher robustness, supporting loads up until similar slips, presenting a more resilient pull-out behaviour [9]. Zhao et al. embarked on a comprehensive investigation into the bond performance of CFRP bars, blending experimental and theoretical approaches. Their study, encompassing the stress–slip behaviour under monotonic and reversed cyclic loading, unveiled a direct link between elevated concrete compressive strengths and enhanced maximum bond stresses. Furthermore, the diameter of CFRP bars and embedment length significantly influenced the regulation of this maximum stress. Notably, the study revealed that under reversed cyclic loading, the maximum bond stresses were diminished compared to monotonic loading under identical conditions, emphasising the susceptibility of CFRP bond to load variations [10]. While much progress has been made, the application of CFRP under the arduous conditions of cyclic loading continues to present a challenge; one that extends beyond traditional means of steel–concrete bonding. The anisotropic behaviour of CFRP, driven by fibre orientation and adhesive matrix properties, demands specialised consideration. This is of particular importance as it governs the primary failure mechanisms—ranging from concrete crushing to FRP rupture—each influenced to varying degrees by the manner of CFRP application [11]. An exploration into the failure modes of CFRP–concrete interfaces under cyclic fatigue provides further perspective. Hao Zhou,

Dilum Fernando, Van Thuan Nguyen, and Jian-Guo Dai, through intensive experimental studies, recognised the onset of damage at the precise point where interfacial shear stress surpassed 80% of its ultimate strength. Various failure modes surfaced, such as cohesion failures within the concrete, adhesive failures, and interlaminar failures within the CFRP itself [12]. Yet, these investigations have stopped short of effectively simulating concrete sections embedded with CFRP rods, owing mainly to limited comprehension of the bond characteristics between the CFRP and concrete elements. Such information is pivotal for accurate simulations that could, in turn, guide thoughtful design and implementation practices. Currently, most models are constrained by a "Tie" constraint, a rudimentary and not entirely accurate representation of the complex CFRP–concrete interface—especially under the force of cyclic "push–pull" conditions that accentuate fatigue failures [12]. Despite the volume of studies dedicated to unveiling the mechanical and physical traits of CFRP rods for rehabilitation and enhancement applications, significant gaps linger. The influence of variables like embedment length, ambient conditions (temperature and humidity), and various binders utilised has been well-studied [13]. Yet, the understanding of bonding behaviours between CFRP and concrete, specifically under cyclic load conditions that reflect real-world structural pressures, remains a conspicuous lacuna in current research, limiting the simulation's accuracy for concrete embedded with CFRP rods using finite element methods [8]. It is this knowledge gap that this study seeks to bridge. The primary goal is to elucidate the bonding dynamics between CFRP rods and conventional G40 concrete as well as UHPFRC under the specific stresses of cyclic loads. To extend the practical application of this research, a robust analytical model has been developed to accurately simulate and predict the bonding characteristics of CFRP rods embedded in UHPFRC under cyclic loading conditions. An enhanced understanding of these interactions will not only demystify the mechanisms of failure within such composite materials but will also propel the practical application of CFRP in construction, encouraging innovation in the design and longevity of tomorrow's infrastructural giants.

2. Bonding of Embedded CFRP Rod in Concrete G40 and UHPFRC

The initial step in developing an analytical model for the adhesion between CFRP rods and concrete involves assessing the CFRP rod's behaviour when it is embedded in a concrete matrix under applied stress. Given the crucial impact of the bond, especially in situations where the structure undergoes cyclical loading and subsequent unloading, which leads to crack propagation on the contact surface, it is essential to examine the bond integrity of CFRP within two distinct concrete compositions under repeated loading conditions.

2.1. Considered Coupled Concrete Cube Samples Linked with CFRP Rod

Material property and behaviour analyses indicate that the CFRP rod and conventional concrete exhibit limited flexibility under cyclic loading. Conventional concrete demonstrates brittle behaviour, leading to reduced performance and often premature fatigue failure in structures such as bridges and parking facilities. These structures frequently require significant rehabilitation to prevent catastrophic failure.

In contrast, Ultra-High-Performance Fibre-Reinforced Concrete (UHPFRC) not only offers a high strength-to-weight ratio but also increased ductility, mitigating the risk of fatigue failure under cyclic loading. Although CFRP is a brittle composite, its combination with UHPFRC allows for better absorption of dynamic loads, potentially enhancing bond strength compared to its performance with conventional concrete.

In this context, the present study analyses two cubic samples: one comprising conventional Grade 40 concrete and the other with a CFRP rod embedded in Ultra-High-Performance Fibre-Reinforced Concrete (UHPFRC). Finite element simulations were conducted to determine key parameters including stiffness, bond strength, and displacement. These parameters are crucial to refining the analytical model for more accurately simulating CFRP-rod-reinforced concrete under cyclic loads.

The geometric modelling for the double pull-out test specimen was conducted in accordance with specific dimensions to fit the laboratory limitations for the testing setup. Table 1 displays the geometric dimensions of all components. The specified embedment length of 300 mm for both the top and bottom sections of the concrete has been configured to adhere to the conservative guidelines of ACI 440.3R, which tend to overestimate the values [14]. This specification is in line with the findings of T. Tibet Akbaş's research, which suggests the optimal bonding length to be 25 times the CFRP rod's diameter, denoted as "25d" [15,16]. Figure 1 illustrates the test specimen's dimensions, while Figure 2 depicts the complete assembly of the required components.

Table 1. Dimension List of Specimens.

Notation	Length (mm)	Width (mm)	Height (mm)	Embedment Length (mm)	Concrete Cover (mm)
Top Concrete	430	430	400	300 [16]	50
Bottom Concrete	700	700	400	300 [16]	50
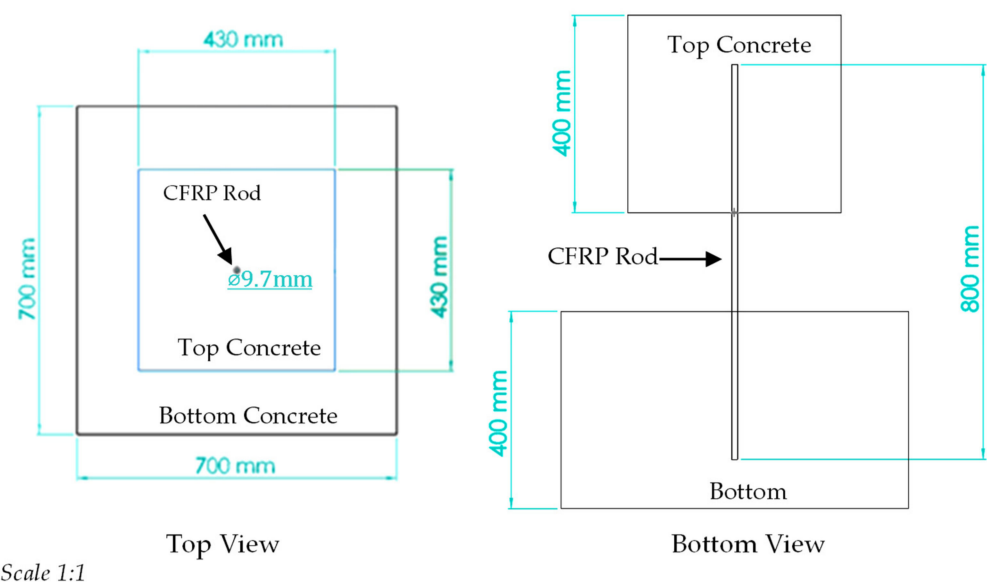
**Figure 1.** Dimension of Top and Bottom Concrete with embedded CFRP Rod.

2.2. Material Properties

2.2.1. Grade 40 Concrete and UHPFRC

In the realm of construction materials, the distinction between conventional concrete and advanced composites plays a pivotal role in determining structural performance. Grade 40 concrete serves as a fundamental starting point. Comprising primarily concrete, steel reinforcement, and a Carbon-Fibre-Reinforced Polymer (CFRP) rod, G40 concrete adheres to well-established practices. It is crafted following a precise recipe to serve as a control specimen, featuring a steel rebar cage with 9 mm diameter rebars intended for pull-out test facilitation. This standard mix, designed in accordance with BS 5328-Part 2 [17], undergoes a standard curing process of 28 days to ensure optimal strength and durability.

In a marked departure from conventional concrete practices, Ultra-High-Performance Fibre-Reinforced Concrete (UHPFRC) emerges as a sophisticated composite material that surpasses the performance of traditional concrete by incorporating a unique blend of steel fibres, superplasticisers, and Ground Granulated Blast Furnace Slag (GGBS), among other additives. These carefully selected constituents coalesce to form an advanced, homogeneous cementitious composite, meticulously engineered to achieve extraordinary compressive strengths exceeding 150 MPa, as elucidated in Table 2. UHPFRC's remarkable properties make it an invaluable asset for the restoration and reinforcement of structural

components that face the rigours of severe environmental and load-related challenges. Its versatility extends to its role as an integral component in the skeletal strength of bridges and skyscrapers. Not only does it fortify structural integrity but also serves as an exceptionally resilient, waterproofing membrane.
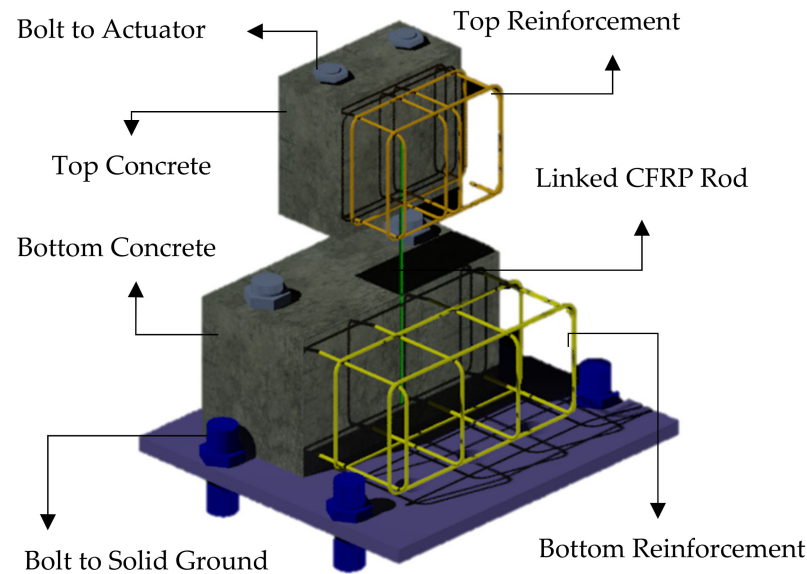
Figure 2. Overall Testing Specimen.

Table 2. Concrete Material Properties.

Material	UHPFRC	G40 Con.
Density (Kg/m^3)	2500	2439
Weight Per Unit Volume (N)	24,520	24,000
Mass/Unit Volume (Kg/m^3)	2500	2400
Modulus of Elasticity (GPa)	45	35
Poisson Ratio	0.2	0.2
Coefficient of Thermal Expansion (Millionths/$^\circ$C)	14.8×10^{-6}	10×10^{-6}

Diving deeper into the reinforcement aspect, the UHPFRC employs copper-coated micro steel fibres (WSF0220), adhering to industry standards such as ASTM A820 [18] and BS EN 14889 [19], with specific fibre details tabulated in Table 3. Habel et al. introduced a fibre factor, a measure that encapsulates both volume fraction and aspect ratio, ranging between 0.8 and 2.0 [20], setting a benchmark for the expected performance of fibre-reinforced composites. Further specifying the operational thresholds, Le Hoang and Fehling recommended strain limits for straight steel fibres to be in the range of 2.5% to 7% [21], underlining the formidable tension-bearing capacity of these discreet yet integral components of UHPFRC.

Table 3. Property of Steel Fibre.

Code	Type	l_f (mm)	d_f (mm)	σ_f (N/m^2)	Shape
WSF0220	Straight	20 ± 1	0.2 ± 0.5	2500	Straight

2.2.2. CFRP Properties

The application of Carbon-Fibre-Reinforced Polymer (CFRP) in structural engineering is highly regarded for its exceptional protective qualities and service life enhancement of structures exposed to severe conditions. Known for its efficient insulation against thermal

fluctuations, moisture penetration, and aggressive chemical agents, CFRP serves as a vital material in safeguarding the integrity of infrastructural components. The manufacturing of CFRP involves an intricate process where carbon fibres are embedded within a resin matrix, the synergy of which imparts the composite material with its notable strength and durability characteristics.

The unique properties of CFRP stem from the interplay between the high tensile strength of the carbon fibres and the binding capability of the resin matrix, which together contribute to the overall robustness and performance of the material under a variety of environmental stimuli. The comprehensive properties of CFRP, which include its mechanical strength, thermal stability, corrosion resistance, and fatigue endurance, are meticulously tabulated in Table 4. This tabulation serves not only as a point of reference but also as a testament to the capabilities of CFRP as a reinforcing and protective agent in modern construction practices.

Table 4. CFRP Properties.

Property	Value	Image
Matrix	Epoxy Resin	
Appearance and Colour	Solid, Round, Grey	
Density (g/cm^3)	1.54	
Fibre Content (%)	74	
Diameter (mm)	9.7	
Flexural Strength (N/mm^2)	2000	
Modulus of Elasticity (GPa)	155	Smooth CFRP Rod
Tensile Strength (MPa)	1685	

The integration of CFRP into construction not only extends the service life of structures but also offers a lightweight yet sturdy alternative to traditional materials. Its versatility is such that it can be applied in numerous contexts, ranging from the restoration of aging infrastructure to the enhancement of new, avant-garde architectural endeavours, effectively meeting both the corrective and prescriptive demands of the industry.

Table 4 therefore is a crucial element of this study, encapsulating the quintessential properties of CFRP, which engineers and researchers can rely upon when designing structures to withstand the rigours of harsh environments and to optimise the durability and longevity of the built environment.

3. Development of Finite Element Model for G40 Concrete and UHPFRC Using Non-Interface Element

Numerical analysis via the Finite Element Method (FEM) is conducted to evaluate the bond strength between Carbon-Fibre-Reinforced Polymer (CFRP) and concrete in the absence of interface elements. The FEM software Abaqus/CAE v. 2022 is utilised to model the CFRP pull-out test for both Grade 40 concrete and Ultra-High-Performance Fibre-Reinforced Concrete (UHPFRC). Additionally, a microanalysis of the pull-out test was performed, considering scenarios with and without an interface element, as analytically formulated in this study.

3.1. Property Assignment

3.1.1. Concrete Damaged Plasticity (CDP) Mechanism

The Concrete Damaged Plasticity (CDP) constitutive model is particularly sensitive to deformation in zones lacking a reinforcement mesh. This model assumes that the principal failure mechanisms in Grade 40 concrete and Ultra-High-Performance Fibre-Reinforced Concrete (UHPFRC) are flexural cracking and compressive crushing of the concrete material. It is imperative to acknowledge that the absence of a reinforcing mesh significantly influences the predictive accuracy of the CDP model, an aspect essential for understanding the structural behaviour of concrete [22].

3.1.2. Properties of CFRP

Composite materials such as Carbon-Fibre-Reinforced Polymer (CFRP), consisting of fibres embedded in a resin matrix, are typically treated as orthotropic due to their directional mechanical properties, notably the Young's modulus. Accurate analysis requires data that can predict stress, forces, torque, and potential damage within the CFRP material. In the current model, however, the elastic properties of CFRP were assumed isotropic for simplification, meaning they exhibit uniform behaviour in all directions, which is a deviation from the orthotropic nature typically found in these composites. For the Three-Dimensional (3D) modelling of the CFRP rod in this study, "engineering constants" were employed to define these isotropic properties, with the relevant data presented in Table 5.

Table 5. CFRP Finite Element Properties.

E_{11} (MPa)	E_{22} (GPa)	$Nu_{12} = Nu_{13}$ (GPa)	Nu_{23} (GPa)	$G_{12} = G_{13}$ (GPa)	G_{23} (GPa)	Density (Tonne/mm^3)
130,000	8000	0.28	0.4	6	3.7	1.56×10^{-9}

3.1.3. Constitutive Model of Steel Reinforcement Bars

At low strain magnitudes, steel reinforcement bars typically demonstrate a nearly linear elastic response, with the elastic modulus remaining constant, as elaborated in Table 6. Upon experiencing increased stress magnitudes, steel reinforcement bars begin to display inelastic and non-linear characteristics, a behaviour commonly known as plasticity. For the scope of this research, the plastic behaviour of steel is simplified to a linear representation. This simplification is made under the assumption that the detailed post-yield behaviour of steel reinforcement embedded in concrete is beyond the study's purview. Table 7 provides a summary of the linear plastic criteria adopted to describe the stress–strain relationship for steel within the context of the analysis.

Table 6. Steel Reinforcement Properties.

| Mass Density of Steel (Kg/m^3)	Young's Modulus (N/mm^2)	Poisson Ratio
8050	200,000	0.3

Table 7. Plastic Criteria of Steel Stress–Strain Relationship.

Yield Stress (MPa)	Plastic Strain
200	0
246	0.0235
294	0.0474
374	0.0935
437	0.1377
480	0.18
480	0.18

3.2. Mesh Discretisation

In this simulation, concrete elements are conceptualised as a homogeneous material with support structures incorporating embedded elements, yet they feature a blind hole for the CFRP bar at both the top and bottom of the concrete. The modelling strategy adhered to a standardised, fine mesh with a global size of 20 mm, as depicted in Figure 3a. The specimens were discretised using eight-node, reduced-integration brick elements (C3D8R) for the concrete and two-node link elements (T3D2) for the steel reinforcement bars. Each C3D8R element has eight nodes with three degrees of freedom, making it suitable for 3D modelling of solids, with or without reinforcement. This element is adept at simulating concrete tension cracking, compression crushing, creep effects, and accommodating large

strain. Conversely, T3D2 elements are designated for one-dimensional reinforcement bars that primarily undergo axial deformation. The blind holes in the concrete were meticulously meshed using a seeding tool to achieve a finer mesh resolution. The partitioning of the model was employed to ensure a more precise mesh that promotes optimal bond strength and effective load transfer within the system. The CFRP rod was also subjected to meshing as a three-dimensional element with a 15 mm mesh size, as illustrated in Figure 3b.
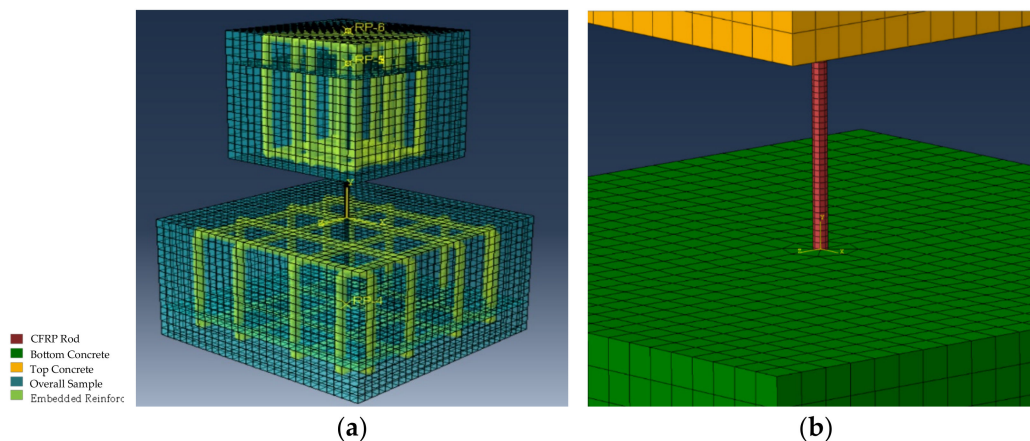
Figure 3. (**a**) Mesh of Concrete; (**b**) CFRP rod mesh as a 3D element with 15 mm mesh size.

Furthermore, a mesh sensitivity analysis was executed to determine the effect of mesh size on the outcomes. Although finer meshing is typically anticipated to produce more accurate results, the analysis revealed that mesh sizes ranging from 5 mm to 20 mm provided similar results. Thus, to curtail computational processing time and minimize roundoff errors, a mesh size of 20 mm was selected as standard. It is important to emphasize that the ideal mesh size is inherently dependent on the specifics of the model, indicating that different models may necessitate different optimal mesh sizes. With this refined understanding of the mesh size, sensitivity analysis has been duly integrated into the discussion to clarify the methodological choices made during the modelling process.

3.3. Interactions

To compare the commonly assumed "Tie" interaction between CFRP and concrete found in most literature studies with the newly developed interface element investigated in this article, two numerical models were constructed. One interaction scenario involved embedding CFRP rods directly into the concrete without utilising an interface element, while the other employed an interaction definition based on analytical results and stiffness values derived from experimental data. The interaction between CFRP bars partially embedded in both concrete segments required a distinct approach, namely, partitioning. Since CFRP is considered an external reinforcement to concrete, full embedment akin to conventional reinforcement is not viable; however, perfect bonding between CFRP and concrete is essential. Consequently, for the CFRP–concrete interaction, the concrete section was partitioned into four pieces, and the externally extruded hole for CFRP was sealed. The Tie interaction between these segments was implemented with the surface-to-surface discretisation method (Figure 4). This approach allows the CFRP bar to exhibit behaviour consistent with testing and material properties within the concrete layers. Additionally, Table 8 summarises the contact behaviour parameters. Similarly, for UHPFRC and normal G40 concrete, the same modelling and simulation approach was employed, with the only difference being the material properties.
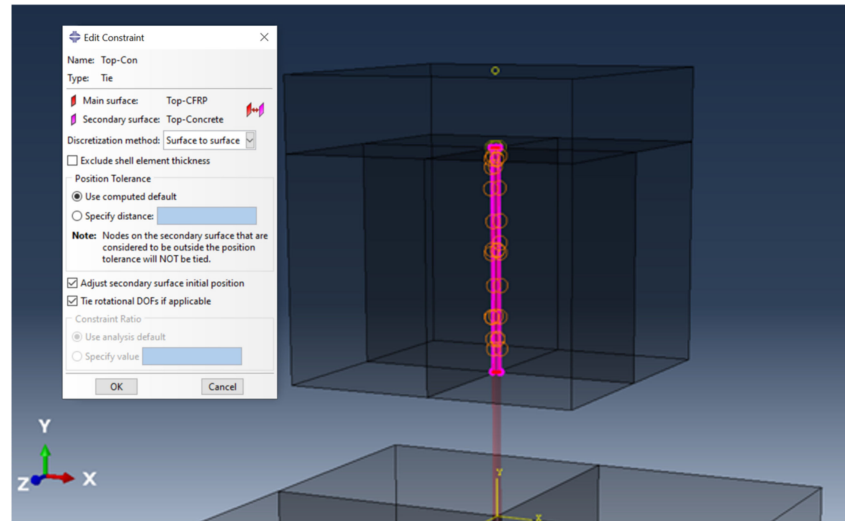
Figure 4. CFRP Interaction with Concrete Member Without Interface Element.

**Table 8.** Interaction Parameters for Non-Interface Element.

Tangential Behaviour	Shear Stress	Normal Behaviour
0.3	5.9	"Hard" Contact

3.4. Boundary Conditions

The boundary conditions were applied by fixing the bottom concrete in all directions and restraining the top concrete in the x- and y-directions while allowing movement along the z-axis with upward loading (Figure 5a). A load displacement of 5 mm was applied with a tabular amplitude to define the cyclic behaviour of the displacement loading. Displacement control loading was employed, wherein displacements were applied rather than directly applying loads to the model. The amplitude shown in Figure 5b represents a cyclic test conducted in compliance with ASTM standards to investigate the model's behaviour under applied axial loads using displacement control at an amplitude of 2 mm. force–displacement data were developed adhering to the ATC-24 code [23].
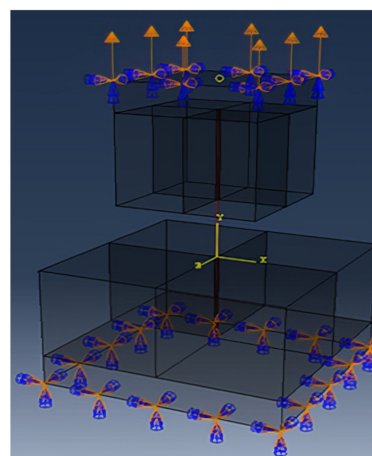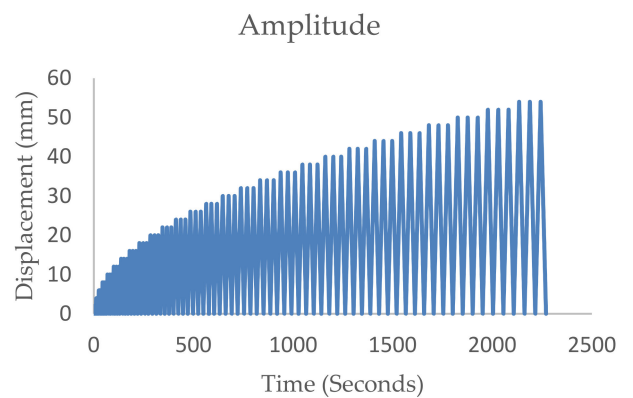
(**a**)   (**b**)

Figure 5. (**a**) Boundary setup with fixed bottom and semi-fixed top concrete under upward load. (**b**) Cyclic test force–displacement curve with 2 mm-controlled displacement per ATC-24 [23].

3.5. Finite Element Analysis Result and Discussion

The simulations were replicated for Grade 40 concrete as well as UHPFRC. The cyclic load was applied to the CFRP embedded within the top concrete, while the bottom concrete remained restrained on the ground. The results shown in Figure 6a depict the areas and nodes subjected to the highest displacement, and Figure 6b illustrates the accumulated stress distribution. The magnitude of plastic strain is visualised in Figure 7a and the equivalent plastic strain is displayed in Figure 7b.

| (a) | (b) |
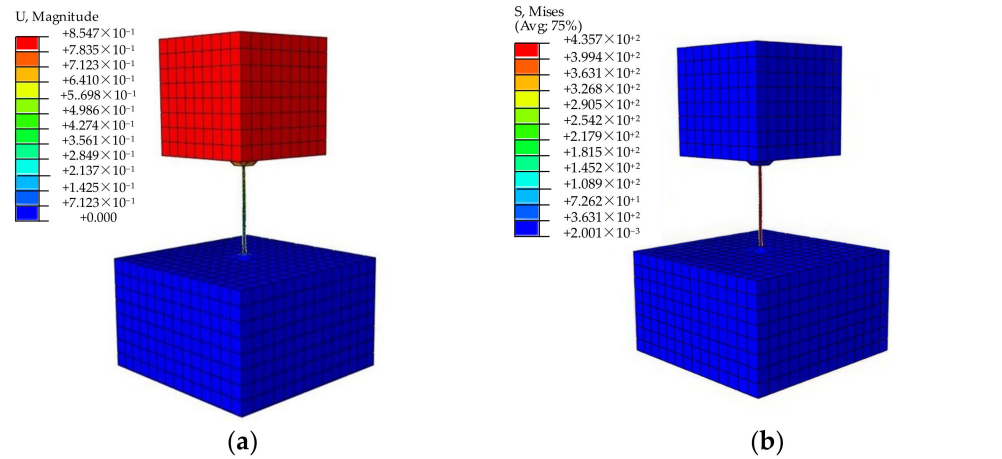
Figure 6. Numerical Analysis (Abaqus): (**a**) Displacement Magnitude; (**b**) Strain and Stress.
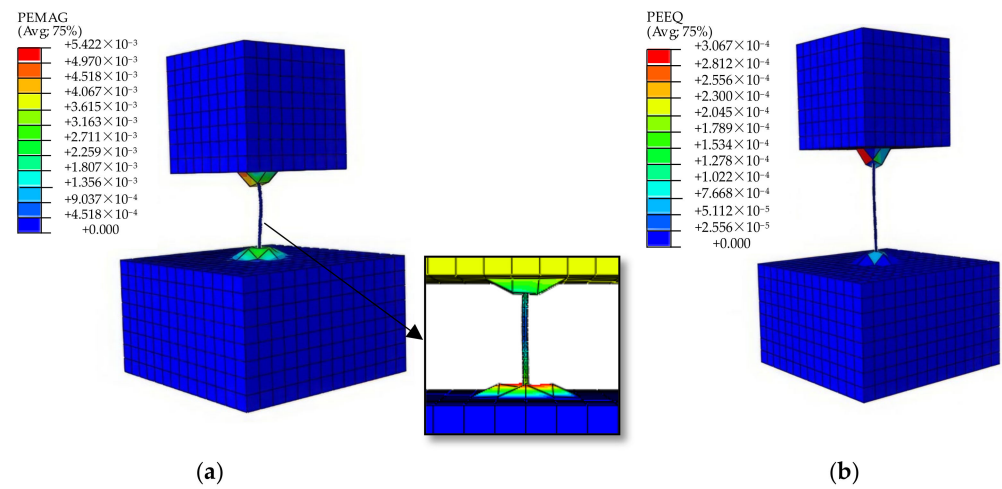

| (a) | (b) |

Figure 7. Numerical Analysis (Abaqus): (**a**) Magnitude of Plastic Strain; (**b**) Equivalent plastic strain.

An analysis of the load–displacement curve presented in Figure 8 reveals significant insights into the behaviour of G40 concrete under cyclic loading. Notably, the force reaches a peak of 33.66 kN at a displacement of 6 mm. In contrast, the load–displacement curve for UHPFRC specimens exhibits more promising results. The force–displacement relationship indicates a resilient cyclic loading response accompanied by substantial energy dissipation. While the maximum force approaches 70 kN at an 9.14 mm displacement, the bond remains intact, and debonding occurs on average at 9.39 mm. Despite the force diminishing due to debonding at the tip of the CFRP in the bottom concrete, the surface of the CFRP rod in contact with UHPFRC continues to withstand the cyclic loading.
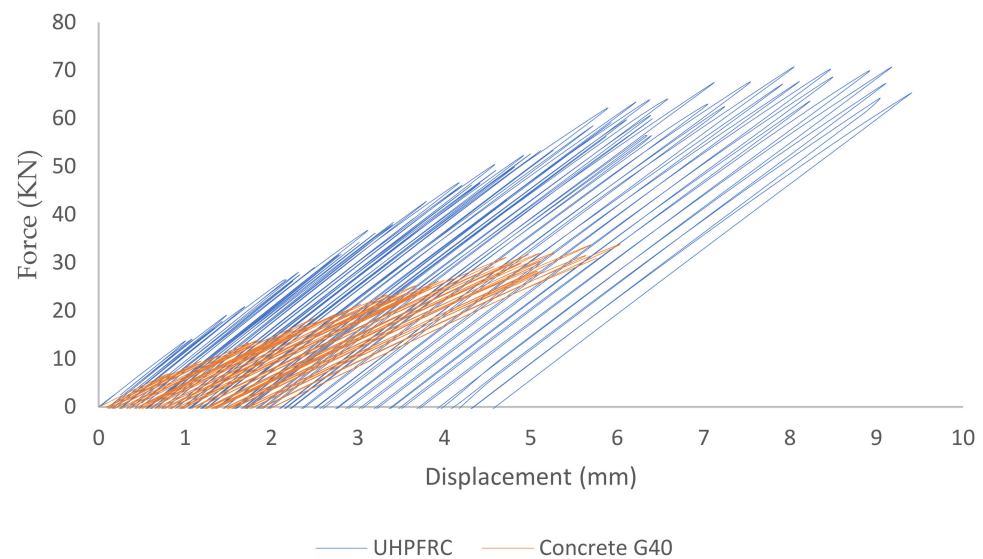
Figure 8. Force–Displacement of G40 Concrete vs. UHPFRC.

4. Experimental Double Pull-Out Test on G40 Concrete and UHPFRC

The pull-out test on prototypes prepared with Grade 40 concrete and UPHFRC was conducted to assess the bonding between CFRP and concrete. Various factors can influence the data and results, potentially leading to inaccurate or unreliable outcomes. The concrete material itself is a critical element that can impact bonding strength. The excessive use of coarse aggregate with sharp or irregular shapes can create significant voids between the interlocking contact points of the concrete and CFRP, resulting in weak bonding. The more homogenous the concrete composition, the better load transfer that can occur.

In addition to concrete material, the rate of loading, which corresponds to the amplitude, also plays a significant role. The amplitude must be gradually increased to avoid sudden pull-out or push-in effects that could compromise the test results. The presence of any existing flexural or shear cracks can also lead to premature failure. Other factors such as environmental conditions, laboratory setup, and even geometry can also influence the test outcomes.

This test was specifically designed to examine the CFRP bonding without the assistance of additional methods, such as using epoxy binders. Subsequently, a cyclic pull-out test was performed to assess the force required to debond the CFRP or cause the CFRP material to reach its tensile yielding point. Since the ACI does not provide specific guidelines for this type of procedure, the JSCE C1.101 guidelines were utilised for the design and construction of concrete structures reinforced with fibre materials [24].

The experimental setup employed the RILEM/CEB/FIP (1994) [25] arrangement, involving the fabrication of two cubic specimens. The top cube measured $400 \times 400 \times 430$ mm, while the bottom specimen measured $700 \times 700 \times 430$ mm. Both specimens were prepared by embedding a CFRP rod in both the top and bottom concrete, enabling the execution of a cyclic pull-out test. To validate the experimental results, comparisons were made with the outcomes obtained from FEM software simulations.

The initial design for a double pull-out test for G40 concrete and UHPFRC prototypes was conducted under a cyclic loading actuator, as illustrated in Figure 9. The concept involves a CFRP rod embedded in both the top and bottom concrete blocks. The bottom concrete was fully restrained on the ground using bolts and nuts, while the top concrete was attached to a dynamic actuator that performed the pulling action.

4.1. Experimental Testing

Cyclic pull-out tests were conducted on G40 concrete prototypes as a benchmark and UHPFRC as the target specimen to evaluate the CFRP–concrete bonding interface. The

obtained results were recorded using the operator data logger, along with data collected from strain gauges. The bottom concrete served as a support, while the top concrete, where the load was applied, acted as a pull-out shaft to detach the CFRP from the bottom concrete (Figure 10).
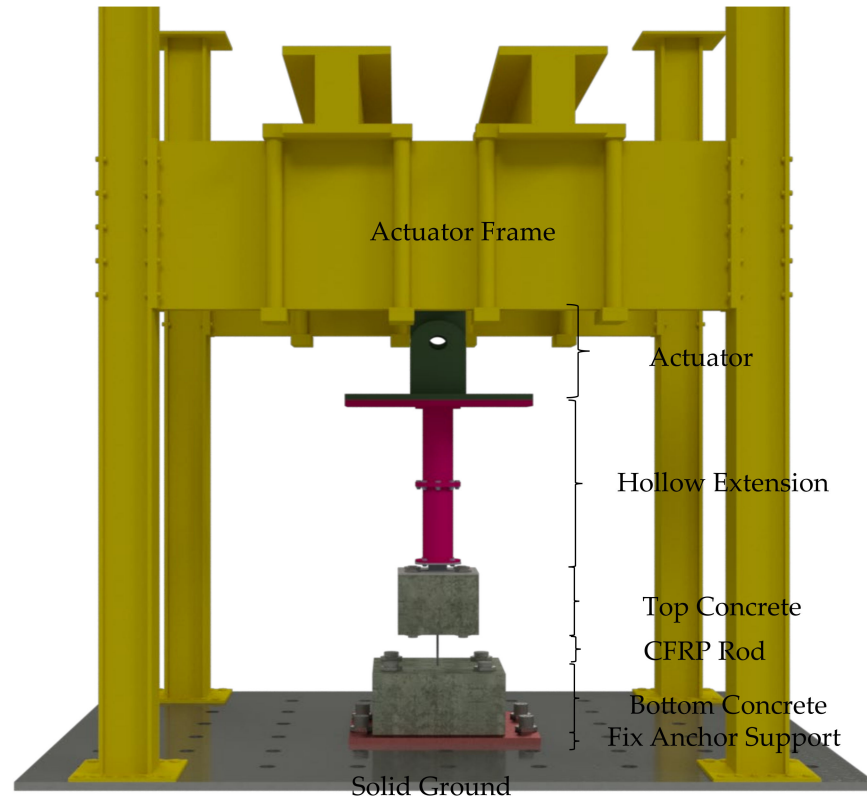

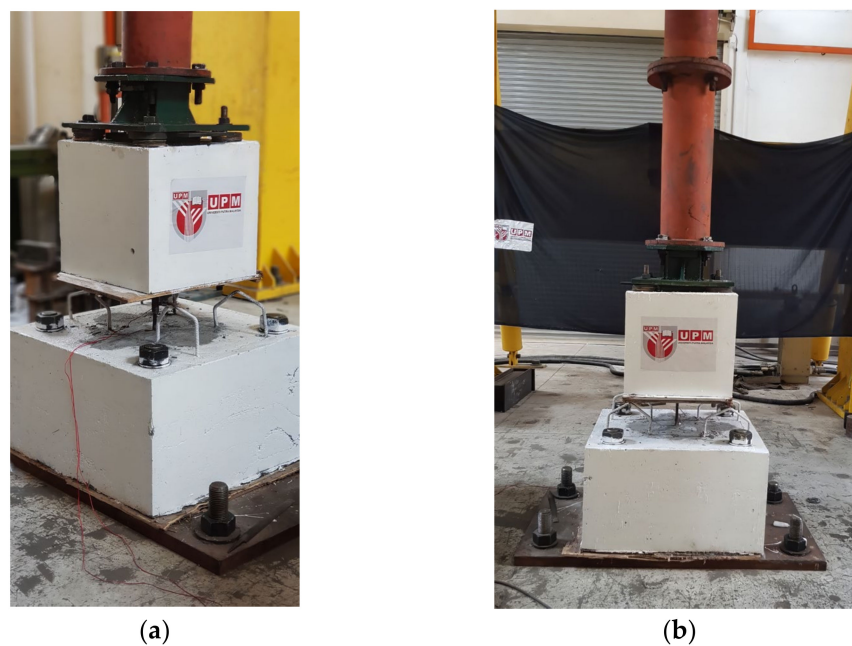**Figure 9.** Testing Setup Schematic.

Figure 10. Test Specimen Under Cyclic Actuator: (**a**) G40 Concrete; (**b**) UHPFRC.

4.2. Experimental Test Result Analysis

4.2.1. Mechanical Test Result

The evaluation of concrete compressive strength is crucial for ensuring the structural integrity of construction materials. The global standard BS EN 12390-3:2002 [26] emphasises the rigorous methodologies employed in this assessment. Adhering to precise specimen dimensions, calibrating compressive testing machines with specified failure load parameters (20% to 80% of full scale), and maintaining a stringent ±1% relative error tolerance are critical aspects of the compressive strength testing process [27,28]. The compressive mechanical test was conducted using a MATEST (MTS) machine. The compressive stress trend up to the first crack was observed for all the specimens and continued with full failure. According to BS EN 12390-3 "Typical Failure Mode of Test Specimen", G40 concrete exhibited a semi-explosive failure mode (Figure 11a), while UHPFRC displayed a more robust, non-explosive failure mode (Figure 11b). This characteristic is more desirable for structural applications [26]. Ultra-High-Performance Fibre-Reinforced Concrete (UHPFRC) demonstrates significantly greater strength than conventional concrete. It undergoes a rapid evolution of mechanical properties over time, achieving high early-age strength and stiffness, with a short-term hydration regime that is nearly complete within 90 days [20]. Experimental tests on UHPFRC have revealed substantial improvements in both compressive and flexural strengths [29]. The mechanical test results for G40 concrete and UHPFRC are presented in Figure 12. UHPFRC specimens were found to be more elastic, with 90–95 percent of the compressive strengths remaining elastic after strain hardening up to the maximum peak strength. This behaviour, however, is not consistently observed in all UHPFRC specimens and is related to the interaction between the steel fibres and the binder matrix. The ultimate outcome is ductile failure, and the concrete surfaces remain smooth even after strength loss.

(**a**)   (**b**)
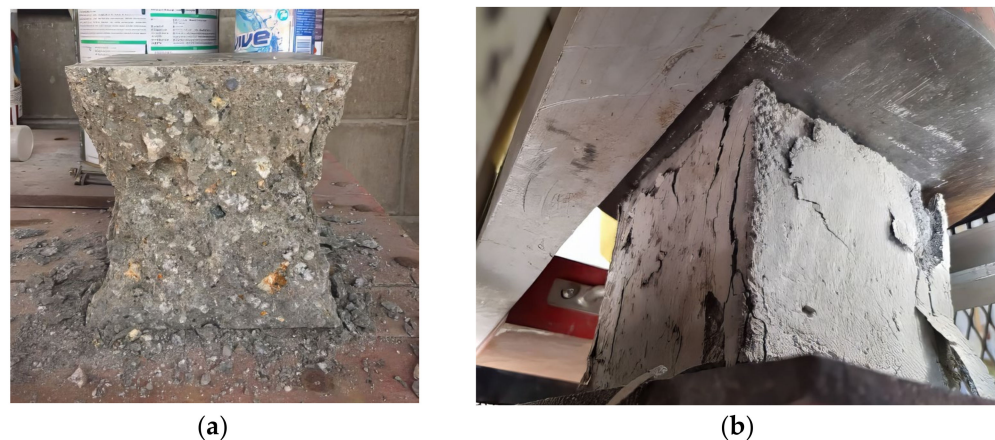
Figure 11. Failure Mode of Test Specimen: (**a**) G40 Concrete; (**b**) UHPFRC.

4.2.2. Double Pull-Out Test Result

The experimental setup for both concrete and UHPFRC followed the same procedure and amplitude. Initial observations were conducted throughout the testing procedure. The observation result of G40 concrete revealed debonding of CFRP of 10.18 mm (Figure 13a). Despite the strain gauges and cyclic actuator collecting data of force–displacement and stress–strain, observations were necessary to monitor the behaviour of CFRP rod bonding.

The cyclic pull-out test on UHPFRC exhibited a distinct behaviour compared to the G40 concrete. As anticipated, UHPFRC exhibited superior force–displacement characteristics compared to G40 concrete. Moreover, the observation on the bonding of CFRP indicated that the CFRP experienced minimal displacement and ultimately failed due to the CFRP material itself, rather than debonding from the UHPFRC (Figure 13b). This experiment provides compelling evidence of the superior interlocking between the CFRP rod and UHPFRC, attributed to the finer particle matrix of UHPFRC compared to conventional

Grade 40 concrete, which contains coarse aggregate. Another factor is the ductility and flexibility of UHPRC, in contrast to the brittleness of G40 concrete. The ductility of UHPFRC enables movement and displacement of the CFRP under cyclic load without failure or debonding. The material interlocking will move up and down as the cyclic load causes the CFRP to undergo push and pull criteria.
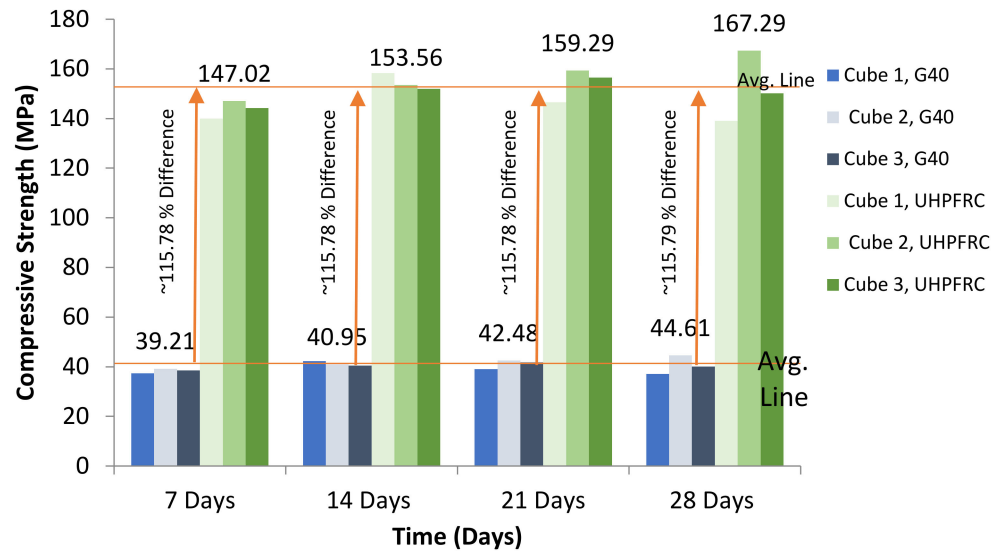

Figure 12. Test Result Comparison of G40 Concrete and UHPFRC.

Figure 13. Debonding/Failure of CFRP–Concrete Element: (**a**) G40 Concrete; (**b**) UHPFRC.

The maximum displacement was recorded at 3269 s, reaching 10.18 mm before debonding fully at 3298 s. Figure 14a shows the time–force graph, indicating a maximum force of 11.53 kN achieved at 2469 s. The force then oscillated until the pull-out failed at 3298 s, terminating the experiment. This maximum force can be attributed to the debonding of the CFRP rod from the concrete base element.

For the UHPFRC specimen, Figure 14b shows the time–force graph, with a maximum force of 41.5 kN achieved at 3103 s. The force continued to oscillate until the pull-out was fully complete at 5356 s, marking the end of the experiment. The maximum force in this case can be attributed to the debonding of the CFRP rod from the UHPFRC base element.

A comparison of the results between the G40 concrete control specimen and the UHPFRC test prototype was conducted (Figure 15 and Table 9). The hypothesis, which aimed to validate the superior performance of UHPFRC compared to G40 concrete, was upheld. This is due to the higher ductility and strength of UHPFRC, the finer interlocking mesh resulting from the absence of coarse aggregate, and the resulting improved bonding.
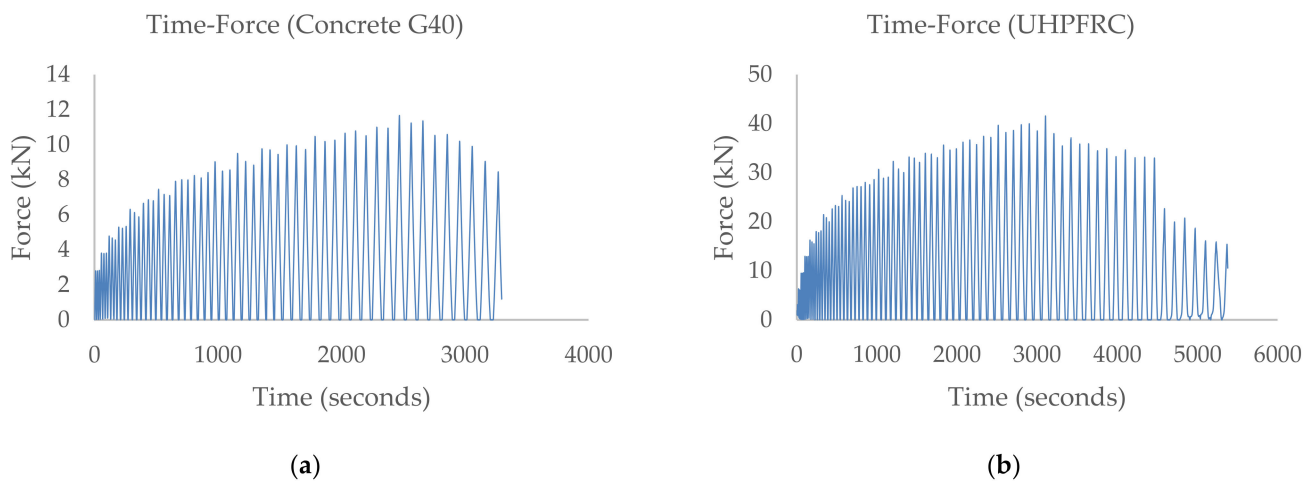
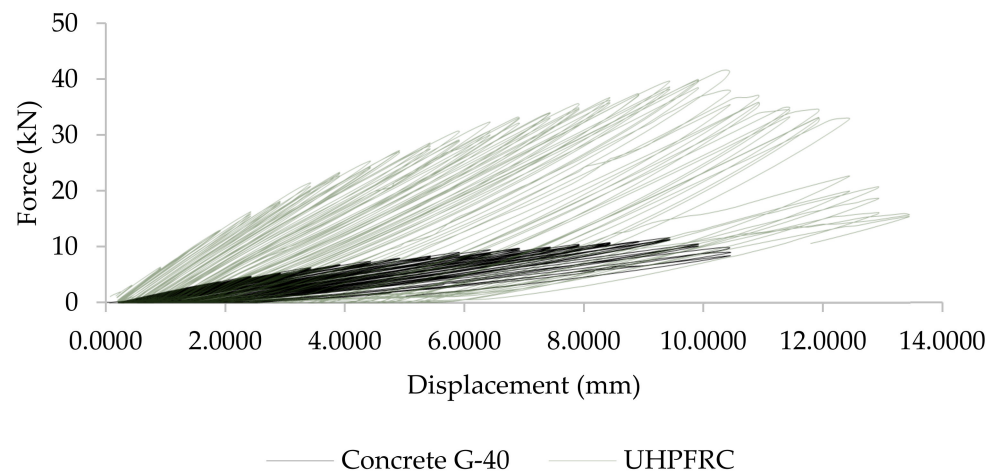**Figure 14.** Time–Force Result: (**a**) G40 Concrete; (**b**) UHPFRC.

Figure 15. Force–Displacement Result of G40 Concrete vs. UHPFRC.

Table 9. Comparison Of Force–Displacement Experimental Result Between G40 Concrete and UHPFRC.

	Displacement (mm)	Force (kN)
G40 Concrete	9.4	11.5
UHPFRC	10.4	41.5
Discrepancy (%)	10.10%	113.2%

4.2.3. Strain Gauge Results

For a thorough testing procedure, accurate and homogenous load transfer was essential. To validate the load transfer uniformity, strain gauges were employed. Three strain gauges (bottom: SG1, middle: SG2, and top: SG3) were installed on the CFRP and connected to the data logger to record strain data (Figure 16).

The strain gauge results for G40 concrete and Ultra-High-Performance Fibre-Reinforced Concrete (UHPFRC) are presented in Figures 17 and 18, respectively. The strain behaviour at SG1 and SG3, located at the bottom and top, respectively, exhibits remarkable consistency. However, SG2, positioned in the middle, records the highest strain. The central region of the CFRP rod, near SG3, serves as the yielding point, exhibiting the highest strain increment of 466 and corresponding strain value of 0.0013. Similarly, SG1 and SG3 exhibit peak values of 466 strain increment and strain of 0.00098, respectively. This trendline depicts a gradual increase in strain up to the peak point, followed by a subsequent decline (Figure 17). This

trend suggests an efficient force transfer between the CFRP rod and concrete interface. Beyond strain increment 1302, the strain reduction indicates debonding.
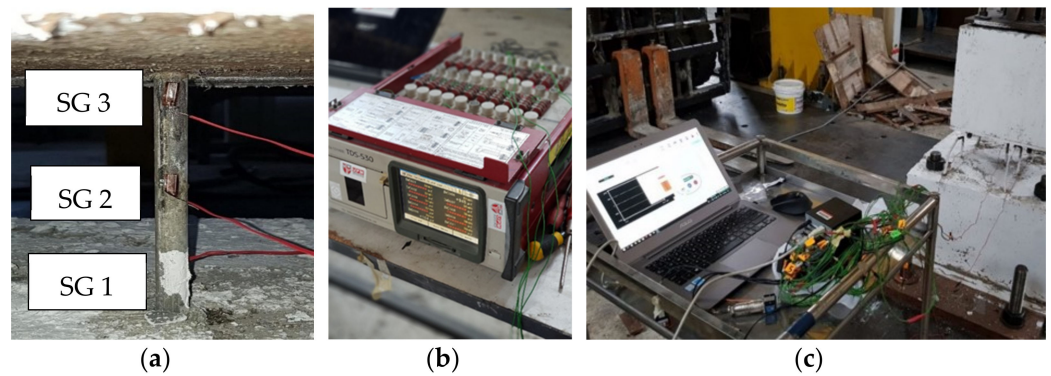

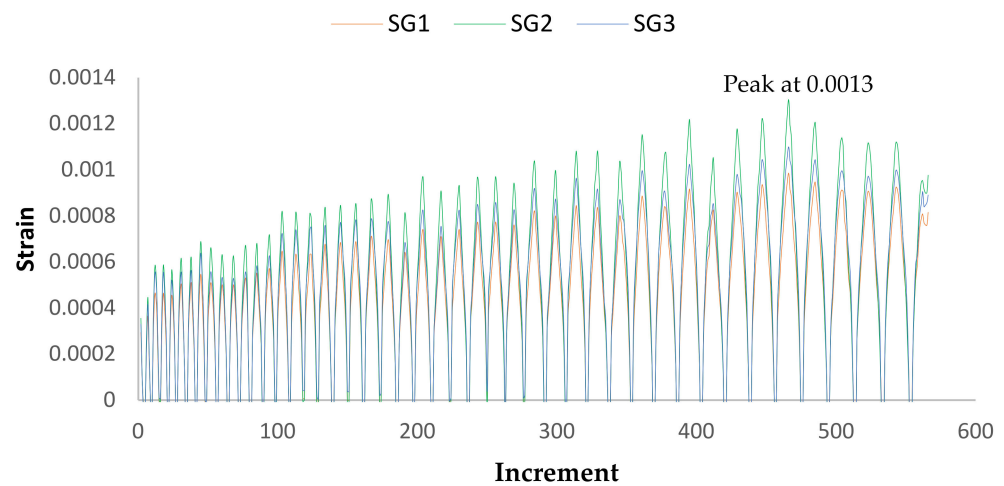**Figure 16.** (**a**) Strain Gauges; (**b**) Data Logger; (**c**) Data Collection.

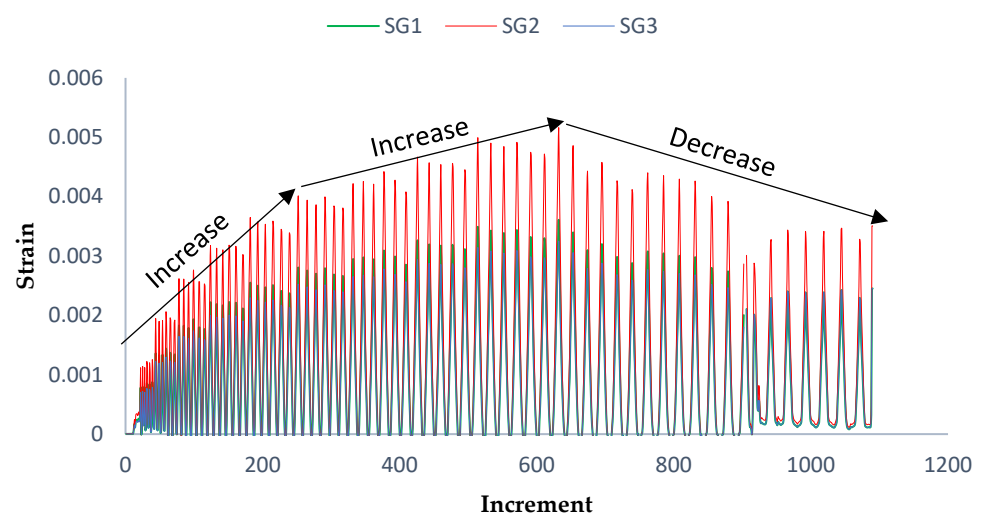**Figure 17.** Strain–Time Graph of G40 Concrete.

Figure 18. Strain–Time Graph of UHPFRC.

In comparison, UHPFRC outperforms G40 concrete, as illustrated in Figure 18. The peak strain value for UHPFRC reaches an impressive 632 at the middle of the CFRP, demonstrating superior performance. The bottom and top strain gauges (SG1 and SG2, respectively) in UHPFRC exhibit identical behaviour, peaking at 632. The effect of cyclic

load, following ACT-24 guidelines, is evident, with an abrupt increase up to peak point No.1, a gradual rise up to peak point No.2, and subsequent strain reduction, indicating diminished CFRP efficiency [23].

The percentage differences clearly demonstrate the remarkable enhancement in force transfer efficiency and sustained cycles for UHPFRC compared to G40 concrete. Notably, UHPFRC exhibits a marked improvement in peak values for SG1 and SG3, with a significant increase from 466 to 632. Similarly, the peak value at SG2 (considered the yielding point) showcases a notable improvement, further supporting the overall superior performance of UHPFRC.

Table 10 provides a detailed comparison of Strain Gauge Differences between G40 Concrete and UHPFRC. The peak values, incremental changes, and strains for SG1, SG2, and SG3 are presented for both materials. The data illustrates a substantial percentage difference, with UHPFRC outperforming G40 concrete across all parameters.

Table 10. Comparison of Strain Gauge Difference (G40 Concrete vs. UHPFRC).

Peak Value	Increment SG1	Strain SG1	Increment SG2	Strain SG2	Increment SG3	Strain SG3
G40 Concrete	466	0.00098	466	0.0013	466	0.0011
UHPFRC	632	0.0032	632	0.0051	632	0.0032
% Difference	30.23	101.53	30.23	118.75	30.23	97.67

5. Comparison and Validation of Experimental and FEM Result for G40 Concrete and UHPFRC Prototype without Interface Element

To verify and authenticate the obtained results from both experimental and numerical studies, a comparison study has been conducted, with the results tabulated in Table 11 to showcase the differences in performance between UHPFRC and G40 concrete. Table 11 also provides a comparison of experimental results against numerical results for validation purposes.

Table 11. Force–Displacement Comparison Between Experimental and Numerical Results for G40 Concrete and UHPFRC.

	Type	Force (kN)	Error (kN)	Difference (%)	Displacement (mm)	Error (mm)	Difference (%)
UHPFRC	Experimental	41.5			10.4		
	Numerical with "Tie" Interface	70	28.5	51.12	9.14	1.26	12.89
G40 Concrete	Experimental	11.5			9.4		
	Numerical with "Tie" Interface	33.6	22.1	98	6	3.4	44.15

The analysis of the revised table reveals significant discrepancies between experimental and numerical results for both UHPFRC and G40 concrete. In the case of UHPFRC, the experimental force of 41.5 kN is noticeably lower than the numerical force of 70 kN, translating to a substantial 51.12% difference. The accompanying displacement data exhibit an even larger difference of 12.89, highlighting a remarkable deviation in predictions.

For G40 concrete, the experimental force of 11.5 kN is significantly lower than the numerical force of 33.6 kN, resulting in a remarkable 98% difference. The associated displacement values further emphasise the substantial disparity, with a 44.15% difference.

While the discrepancies in force measurements are substantial, the numerical model appears to provide relatively accurate predictions for displacement. This analysis underscores the critical need to refine the numerical model, particularly in identifying and addressing sources of error that are impacting force calculations. Recognising these significant discrepancies highlights the urgency for implementing an interface element in the numerical model to minimise such substantial differences. This research aims to fulfil this

objective by providing an interface element to enhance the accuracy of predictions and mitigate discrepancies between experimental and numerical results.

6. Analytical Approach

Currently, sophisticated software is utilised to analyse complex structural elements with respect to their geometry and simulate the behaviour of a particular structure under specific scenarios. However, it is essential to grasp the functioning of such software. Most simulation software in engineering is built upon analytical calculations, which have been extensively studied mathematically over time. With the advent of computers and artificial intelligence, the computation of complex formulas has become significantly more straightforward. Analytical models are employed to comprehend the behaviour of such elements within structures, which are inherently quantitative in nature. However, analytical modelling is restricted to simple geometry elements, and the complexity in geometry would render analytical calculations extremely challenging. For the models employed in this research, the boundary conditions between CFRP and concrete are a few elements that render this analytical model difficult. Additionally, another noteworthy limitation is the inability to model non-linear behaviour [30].

6.1. Modelling Elements

The selection of appropriate modelling elements in FEM analysis is crucial. The bond behaviour between the CFRP rod and concrete is partially geometry dependent. The chosen elements in this study are the CFRP rod acting as a bar element and the concrete, which is represented using rectangular elements. Since the behaviour of bottom concrete with embedded CFRP is similar to the top concrete with embedded CFRP, only one of the concretes (either top or bottom concrete) is considered for analysis.

The type of element and its geometry can influence the type of meshing, matrix and integration equations, number of nodes, and so on. Plane strain analysis permits strains only in the plane. Therefore, plane strain is a suitable analysis to be used in thick structures of CFRP and concrete elements. Plane strain also provides restraining in the lateral direction and stabilises the element. Figure 19 depicts the conversion of a Three-Dimensional (3D) element to a Two-Dimensional (2D) element. This approach aligns with the procedure employed in numerical studies, where solid elements represent the concrete and CFRP rod, while cohesive elements represent a thin surface as the contact surface between CFRP and concrete elements (Figure 20). Each element's characterisation distinguishes its behaviour from the others.
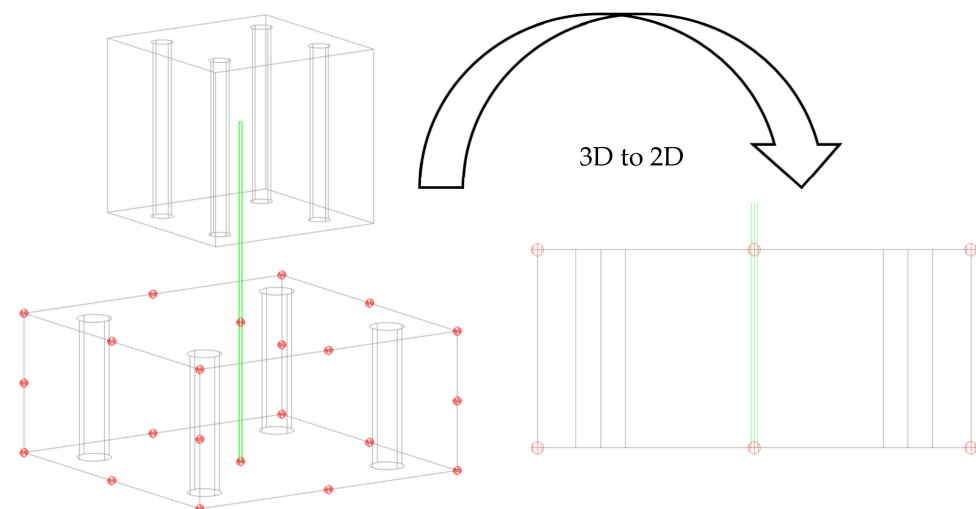
Figure 19. Conversion of 3D 22-node Concrete Specimen To 2D 6-node Specimen.

6.2. Cohesive Elements

Cohesive elements are employed to model the bond between CFRP and concrete, effectively defining the performance of the CFRP rod during pull-out tests. This performance can be influenced by factors such as geometry properties, type of industrial application, testing procedure, and load response. Numerous cohesive element models are available, but the traction separation response model was selected for this study. This model is particularly suitable when the adhesive thickness is negligible or considered zero. It assumes linear bonding performance before crack initiation and allows for the simulation of debonding initiation and damage propagation. This approach places significant emphasis on material properties, making it an excellent choice for simulating the cohesive zone. Although cohesive elements are considered to have negligible thickness, a thin layer was constructed for simulation purposes. This layer was assembled by combining parts with precise nodal coordination, a method particularly useful for forming complex configurations. This part's assembly is illustrated in Figure 20.
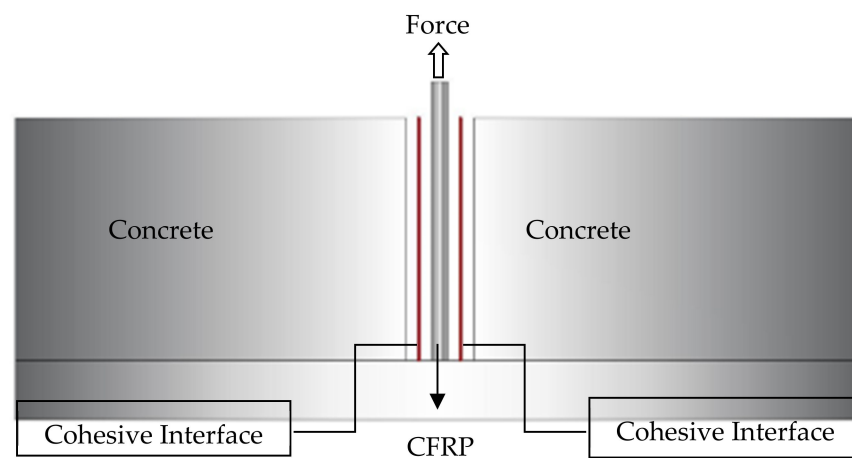
Figure 20. Interface Elements between CFRP rod and Concrete Membrane.

6.3. Solid Elements

Various factors must be considered when selecting appropriate solid elements to model concrete and CFRP. Solid elements are typically used for homogeneous or non-homogeneous composites. However, for this research, both the concrete and CFRP are considered homogeneous. It is essential to note that the steel reinforcement in this research is not represented as a solid element but rather as a wire element. This is because the focus of this research is on evaluating the performance of CFRP, not the steel reinforcement. Therefore, the behaviour of the reinforcement is limited to its role in strengthening the concrete, not its own failure modes.

6.4. Shape Function

The direct stiffness method is employed to compute Degrees of Freedom (DOFs) at the element nodes. The shape function represents the linear displacement field within the element in terms of nodal displacements. The shape function is obtained using the Lagrange method for a 2D solid element, which can be considered as an isoperimetric element. In this case, the shape functions must be written in natural coordinates.

In the finite element approach, the nodal values of the field variable are treated as unknown constants that need to be determined. The interpolation functions are typically polynomial forms of the independent variables, derived to satisfy certain required conditions at the nodes. These interpolation functions are predetermined, known functions of the independent variables, and they describe the variation of the field variable within the finite element.

To determine the stiffness matrix of the element [K], the [B] matrix and [D] matrix of the element need to be generated in advance. Six shape functions have been obtained, as per Table 12, which are crucial components in the [B] matrix.

Table 12. Shape Function of 2D 6-Node element.

Shape Function	Derivation to ξ	Derivation to η	
$N_1 = -1/4\ \xi(1-\xi)(1-\eta)$	$dN_1/d\xi = -1/4\ (1-2\xi)(1-\eta)$	$dN_1/d\eta = 1/4\ \xi(1-\xi)$	(1)
$N_2 = 1/2\ (1-\xi^2)(1-\eta)$	$dN_2/d\xi = -\xi(1-\eta)$	$dN_2/d\eta = -1/2\ (1-\xi^2)$	(2)
$N_3 = 1/4\ \xi(1+\xi)(1-\eta)$	$dN_3/d\xi = 1/4\ (1+2\xi)(1-\eta)$	$dN_3/d\eta = -1/4\ \xi(1+\xi)$	(3)
$N_4 = 1/4\ \xi(1+\xi)(1+\eta)$	$dN_4/d\xi = 1/4\ (1+2\xi)(1+\eta)$	$dN_4/d\eta = 1/4\ \xi(1+\xi)$	(4)
$N_5 = 1/2\ (1-\xi^2)(1+\eta)$	$dN_5/d\xi = -\xi(1+\eta)$	$dN_5/d\eta = 1/2\ (1-\xi^2)$	(5)
$N_6 = -1/4\ \xi(1-\xi)(1+\eta)$	$dN_6/d\xi = -1/4\ (1-2\xi)(1+\eta)$	$dN_6/d\eta = -1/4\ \xi(1-\xi)$	(6)

In general, the number of DOFs associated with a finite element is equal to the product of the number of nodes and the number of values of the field variable (and possibly its derivatives) that must be computed at each node. For this study, with 2 DOFs in both X- and Y-directions and a 2D model comprising six nodes, we have a total of 12 DOFs. Since the considered axes are planar, the 2D element in this research is considered as a plane-strain element.

6.5. [K] Matrix

The element stiffness matrix encapsulates the primary characteristics of a finite element. For a structural finite element, the stiffness matrix incorporates both geometric and material behaviour information, effectively representing the element's resistance to deformation when subjected to external loads. It serves as a crucial determinant of how the element responds to changes in its environment. In the context of CFRP rods embedded in concrete, the stiffness matrix quantifies the interaction between the two materials, dictating their ability to resist deformation and maintain their structural integrity.

$$[k_{concrete}] = \int_{-1}^{+1} \int_{-1}^{+1} [B]^T \cdot [D] \cdot [B] \cdot |J| \cdot t \cdot d\xi \cdot d\eta \tag{7}$$

6.6. Jacobi Matrix

In the Finite Element Method (FEM), the Jacobian matrix of an element connects the quantities expressed in natural coordinate space to their counterparts in real space.

$$\therefore J = \begin{bmatrix} \frac{dx}{d\xi} & \frac{dy}{d\xi} & \frac{dz}{d\xi} \\ \frac{dx}{d\eta} & \frac{dy}{d\eta} & \frac{dz}{d\eta} \\ \frac{dx}{d\zeta} & \frac{dy}{d\zeta} & \frac{dz}{d\zeta} \end{bmatrix} \quad [J] = \begin{bmatrix} \frac{dN_1}{d\xi} & \frac{dN_2}{d\xi} & \frac{dN_3}{d\xi} & \cdots & \frac{dN_{22}}{d\xi} \\ \frac{dN_1}{d\eta} & \frac{dN_2}{d\eta} & \frac{dN_3}{d\eta} & \cdots & \frac{dN_{22}}{d\eta} \\ \frac{dN_1}{d\zeta} & \frac{dN_2}{d\zeta} & \frac{dN_3}{d\zeta} & \cdots & \frac{dN_{22}}{d\zeta} \end{bmatrix} \times \begin{bmatrix} x_1 & y_1 & z_1 \\ x_2 & y_2 & z_2 \\ x_3 & y_3 & z_3 \\ \vdots & \vdots & \vdots \\ \vdots & \vdots & \vdots \\ \vdots & \vdots & \vdots \\ x_{22} & y_{22} & z_{22} \end{bmatrix} \tag{8}$$

The derivatives with respect to global coordinates are computed using the inverse of the Jacobian matrix from local coordinates.

$$\begin{Bmatrix} \frac{dN_i}{dx} \\ \frac{dN_i}{dy} \\ \frac{dN_i}{dz} \end{Bmatrix} = J^{-1} \begin{Bmatrix} \frac{dN_i}{d\xi} \\ \frac{dN_i}{d\eta} \\ \frac{dN_i}{d\zeta} \end{Bmatrix} \quad |J| = \frac{A}{4} = \frac{700 * 400}{4} = 28 * 10^5 \text{ mm}^2 [\text{thickness} = 700 \text{ mm}] \tag{9}$$

The CFRP rod is modelled as a two-node bar element. Subsequently, the constitutive model was incorporated for the two-node bar element within the 12×12 [K_{System}] to ensure compatibility with the concrete element.

$$K_{CFRP} = \begin{bmatrix} \frac{EA}{L} & \frac{-EA}{L} \\ \frac{-EA}{L} & \frac{EA}{L} \end{bmatrix} \quad \begin{array}{c} E = 155,000 \text{ Gpa} \\ I = 73.9 \text{ mm}^2 \\ \text{Length of embedment} = 300 \text{ mm} \end{array} \tag{10}$$

The CFRP rod stiffness matrix (K_{CFRP}) was assembled into the stiffness matrix of the 2D model, which was defined as K_{SYSTEM}. The assembly was performed based on the corresponding nodes, aligning the CFRP's nodal positions with those of the concrete element [31].

$$K_{SYSTEM} = \begin{bmatrix} 0 & 0 & 0 & 0 & 0 & 0 & 0 & 0 & 0 & 0 & 0 & 0 \\ 0 & 0 & 0 & 0 & 0 & 0 & 0 & 0 & 0 & 0 & 0 & 0 \\ 0 & 0 & 0 & 0 & 0 & 0 & 0 & 0 & 0 & 0 & 0 & 0 \\ 0 & 0 & 0 & \frac{EA}{L} & 0 & 0 & 0 & 0 & 0 & \frac{-EA}{L} & 0 & 0 \\ 0 & 0 & 0 & 0 & 0 & 0 & 0 & 0 & 0 & 0 & 0 & 0 \\ 0 & 0 & 0 & 0 & 0 & 0 & 0 & 0 & 0 & 0 & 0 & 0 \\ 0 & 0 & 0 & 0 & 0 & 0 & 0 & 0 & 0 & 0 & 0 & 0 \\ 0 & 0 & 0 & 0 & 0 & 0 & 0 & 0 & 0 & 0 & 0 & 0 \\ 0 & 0 & 0 & 0 & 0 & 0 & 0 & 0 & 0 & 0 & 0 & 0 \\ 0 & 0 & 0 & \frac{-EA}{L} & 0 & 0 & 0 & 0 & 0 & \frac{EA}{L} & 0 & 0 \\ 0 & 0 & 0 & 0 & 0 & 0 & 0 & 0 & 0 & 0 & 0 & 0 \\ 0 & 0 & 0 & 0 & 0 & 0 & 0 & 0 & 0 & 0 & 0 & 0 \end{bmatrix} \tag{11}$$

7. Development of Interface Element

The interface element emerged as a fundamental model that explicitly captures the failure mechanism of CFRP bonding. In finite element analysis, interface elements depict a thin or zero-thickness layer bridging continua. The interface element's constitutive relationship hinges upon a traction–displacement law that generally exhibits elastic behaviour up to a stress-based failure criterion (initiation) and then transitions to softening behaviour, characterised by an area under the curve equal to the critical fracture energy at complete failure (propagation). The formulation of an interface element suitable for planar problems is provided, enabling its linkage with six-node isoperimetric elements possessing rectilinear sides (Figure 21). In the context of planar problems, the geometry of an interface element is represented by a line connecting two solid elements. Deobald L et al. introduced an interface element tailored for analysing delamination fatigue onset or fatigue increase. The authors demonstrated its ability to fully release one or more elements for each time increment while accurately accounting for the number of cycles required to induce fatigue growth over that length [32]. Qian and Xie developed a novel interface element specifically designed to investigate cyclic crack propagation under mixed-mode loading and applied it to analyse an example of cyclic crack propagation under mixed-mode loading [33].

$$N_a = -\frac{1}{2}\xi(\xi - 1) , \ N_b = +\frac{1}{2}\xi(\xi + 1) \tag{12}$$

$$\begin{bmatrix} \Delta_a \\ \Delta_c \end{bmatrix} = \begin{bmatrix} \frac{\Delta u_a}{\Delta v_a} \\ \frac{\Delta u_c}{\Delta v_c} \end{bmatrix} = [\tau]_{(4 \times 8)}[\delta]_{(8 \times 1)} , \ \begin{Bmatrix} \Delta_a \\ \Delta_c \end{Bmatrix} = \begin{bmatrix} N_a & 0 & N_c & 0 \\ 0 & N_a & 0 & N_c \end{bmatrix}[\Delta] = [N][\Delta] \tag{13}$$

$$[N][\Delta] = [N]_\delta = [B_{ij}] = [B_{ij}][\delta] = \begin{Bmatrix} \varepsilon_t \\ \varepsilon_n \end{Bmatrix} , \ \begin{Bmatrix} \varepsilon_t \\ \varepsilon_n \end{Bmatrix} = \frac{1}{t}\begin{Bmatrix} \Delta_u \\ \Delta_v \end{Bmatrix} = [N_\delta]\{\delta\} = [B_{ij}]\{\delta\} \tag{14}$$

$$\varepsilon_{ij} = \frac{\delta_{ij}}{T_o}, T_o = \textit{thickness of interface element} \tag{15}$$

$$[\sigma] = \begin{Bmatrix} \tau \\ \sigma_r \end{Bmatrix} = [D_i]\{\varepsilon\} \, , \; [D] = \begin{bmatrix} k_{ss} & 0 \\ 0 & k_{ns} \end{bmatrix}$$
$$(k_{ss} = 0)$$

(16)

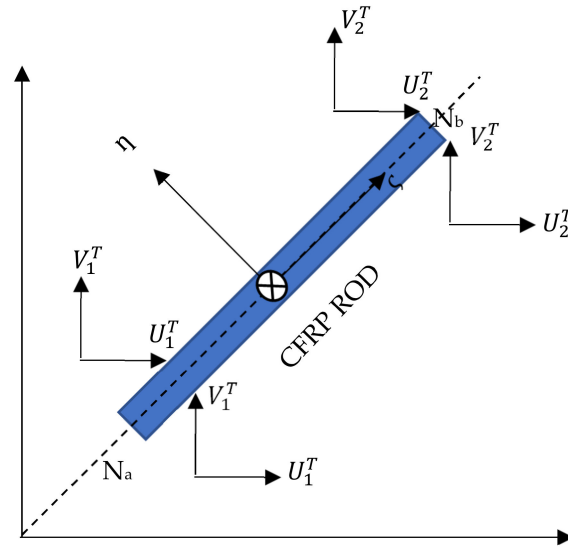$$[K_{system}] = \int [B_i]^T [D_i][B_i]dx$$

(17)

Figure 21. CFRP Linear Contact Interface Element Graph.

As a result, the constitutive stiffness matrix for the interface element, with regard to the embedment length of the CFRP rod in concrete, will be defined by the following equation:

$$[K_{system}] = \int_0^n \begin{bmatrix} B_{11} & B_{12} \\ B_{21} & B_{22} \end{bmatrix}^T \begin{bmatrix} k_{ss} & 0 \\ 0 & k_{ns} \end{bmatrix} \begin{bmatrix} B_{11} & B_{12} \\ B_{21} & B_{22} \end{bmatrix} dx$$
$$n = CFRP \; embedment \; length$$

(18)

Simultaneously, with the [K] matrix obtained from Equation (17), the force–displacement matrix can be derived from the following equation:

$$[F_i]_{2\times 1} = [k_i]_{2\times 2}[\delta_i]_{2\times 1}$$

(19)

8. Implementing of Developed Interface Element in FEM Simulation

Implementation of the developed interface element was employed for the UHPFRC and G40 concrete prototype to assess the formulated CFRP–concrete bonding interaction. An additional adhesive surface was incorporated into the assembly section to define the contact element between CFRP and concrete. The adhesive surface is a thin layer with a negligible thickness of more than zero millimetres, ensuring no impact on the specimen's mass. Utilising the traction–separation constitutive model, surface-based cohesive behaviour provides a simpler approach to simulating cohesive connections with negligibly tiny interface thickness. Surface-based cohesive behaviour adheres to formulas and rules closely resembling those employed for traction–separation behaviour in cohesive components. Linear elastic traction–separation was employed to simulate the adhesive element initially considered in the model. Linear elastic behaviour effectively depicts the onset and progression of damage [34]. The elastic behaviour is described by an elastic constitutive matrix that connects the nominal stresses and strains across the interface.

$$\varepsilon_n = \frac{\delta_n}{T_o}, \varepsilon_s = \frac{\delta_s}{T_o}, \varepsilon_t = \frac{\delta_t}{T_o}$$
(Strain equation in local coordinates)

(20)

$$t = \begin{Bmatrix} t_n \\ t_s \\ t_t \end{Bmatrix} = \begin{bmatrix} E_{nn} & E_{ns} & E_{nt} \\ E_{ns} & E_{ss} & E_{st} \\ E_{nt} & E_{st} & E_{tt} \end{bmatrix} \begin{Bmatrix} \varepsilon_n \\ \varepsilon_s \\ \varepsilon_t \end{Bmatrix} = E\varepsilon \tag{21}$$

(Elastic behaviour matrix for 3D element)

However, the analysis performed on the 2D element solely analyses the Z-direction, which is the direction of loading.

$$t = \begin{Bmatrix} t_n \\ t_s \end{Bmatrix} = \begin{bmatrix} E_{nn} & 0 \\ 0 & E_{ss} \end{bmatrix} \begin{Bmatrix} \varepsilon_n \\ \varepsilon_s \end{Bmatrix} = E\varepsilon \tag{22}$$

(Elastic behaviour matrix for 2D element)

$$E_{ij} = \frac{Young's\ modulus\ in\ normal\ direction}{Thickness\ of\ cohesive\ element} \quad E_{nn} = \frac{1800}{0.2} = 9000$$
$$E_{ss} = \frac{500}{0.2} = 2500 \tag{23}$$

This basic architecture allows for the integration of multiple damage mechanisms that can operate on the same material simultaneously. Each failure mechanism consists of three components: a damage initiation criterion, a damage evolution law, and a decision regarding element deletion when the system reaches a fully damaged state. Damage initiation marks the beginning of degradation in the response of a material point. Degradation commences when the stresses and strains meet specific damage initiation criteria that have been predetermined. Various damage initiation criteria exist, and each damage initiation criterion also has an output variable associated with it to indicate whether the criterion has been met. A value of 1 or higher signifies that the initiation criterion has been fulfilled. In this article, the maximum nominal stress criterion is employed. Damage is assumed to initiate when the maximum nominal stress ratio reaches a value of 1.

$$\max\left\{ \frac{\langle t_n \rangle}{t_n^o}, \frac{\langle t_s \rangle}{t_s^o}, \frac{\langle t_t \rangle}{t_t^o} \right\} = 1 \tag{24}$$

Furthermore, a general contact has been defined as surface-to-surface with minor slip criteria between the CFRP and concrete interface. A "tangential behaviour" with a penalty of 0.3 has been established. Additionally, to preclude any penetration, the normal behaviour has been designated as a rigid "contact". Another interaction has been defined between the CFRP and concrete interface based on the analytical results formulated in this research. The contact property is specified as "cohesive behaviour", which is a thin layer serving as an interface that determines the bonding strength of the CFRP–concrete element. The cohesive behaviour data are presented in Table 13.

Table 13. Cohesive Behaviour Interaction.

K_{nn} (MPa)	K_{ss} (MPa)	K_{tt} (MPa)
1.5	360	360

Additionally, damage initiation parameters with a quadratic traction criterion have been utilised, as shown in Figure 22. The corresponding data are presented in Table 14.

Furthermore, the damage evolution was also considered as linear displacement with a total displacement of 1 mm. This implies that if the bonding at the CFRP–concrete interface exceeds 1 mm, the test is deemed to fail at that point. Additionally, the viscosity is also 1 mm. The normal behaviour was assigned as a rigid "contact", and the tangential behaviour at the CFRP–concrete interface was considered with a friction coefficient of 0.75. The shear stress was specified as 3.9 MPa and the elastic slip was considered as 0.00001. Notwithstanding the general contact that was previously defined, the surfaces of the CFRP that are embedded in concrete will adhere to the cohesive behaviour and are considered exceptions to the general contact to have their own behaviour. Ultimately, the simulation was conducted on two 2D six-node specimens, one with the interface element that was analytically obtained

and the other without an interface element. The maximum stress in Figure 23a indicates that the CFRP rod performs optimally with UHPFRC, with the bonding holding up until the CFRP material itself fails. On the other hand, the displacement results also show that the maximum displacement occurred in the CFRP material while the UHPFRC was also deformed (Figure 23b). The damage propagation in G40 concrete is shown in Figure 24a. The interface at the CFRP has been compromised by 80%, including the tip of the CFRP rod at the inside of the embedded region. The minimal bonding area is caused by angular and coarse aggregate that interlocks with the CFRP, but it is not satisfactory because the debonding exceeds 1 mm. On the other hand, the damage propagation in UHPFRC reveals robust bonding with minimal damage compared to G40 concrete. Notably, no debonding is apparent, attributed to the ductility and interlocking performance of UHPFRC with CFRP rods (Figure 24b).
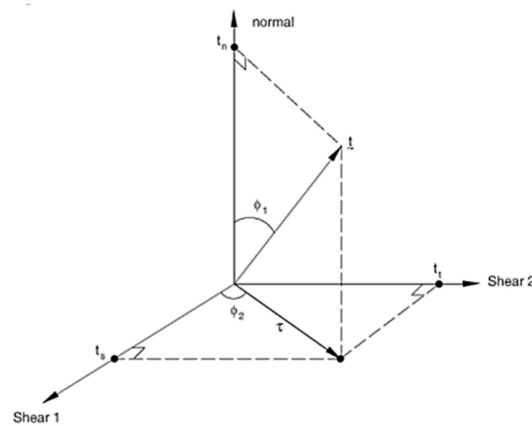

Figure 22. Mixed-mode Measures Based on Quadratic Traction.

Table 14. Damage Initiation Parameter with Quadratic Traction Criterion.

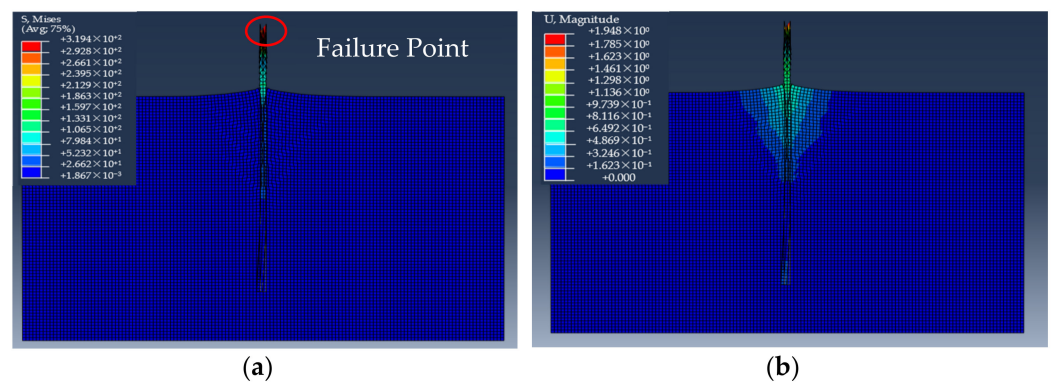| Normal Only (MPa)	Shear-1 Only (MPa)	Shear-2 Only (MPa)
110	9	9

Figure 23. Interface element analysis on UHPFRC. (**a**) Stress; (**b**) Displacement.

The force–displacement curve depicted in Figure 25 illustrates data acquired from the sample with an interface element subjected to cyclic loading for G40 concrete. The maximum force recorded reached 75 kN at a displacement of 12.9 mm. Upon examination of the experimental data for G40 concrete, it became evident that the analytical surface formulated was well-suited for UHPFRC under cyclic loading, as expected, given that the interface element for G40 concrete did not demonstrate any improvement in simulation. It is crucial to note that the primary aim of this study was to enhance the accuracy of the interface element in UHPFRC simulations.
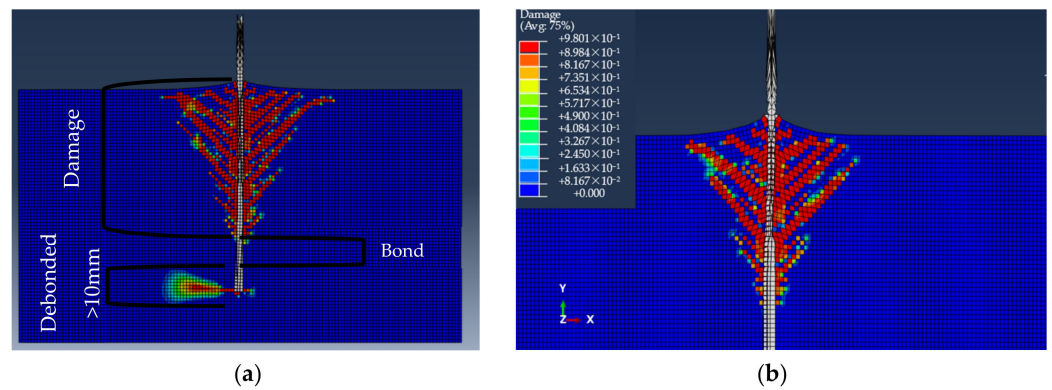
Figure 24. Damage Propagation and Bonding/Debonding Area by CFRP Rod under cyclic Pull-Out excitation in: (**a**) G40 Concrete; (**b**) UHPFRC.
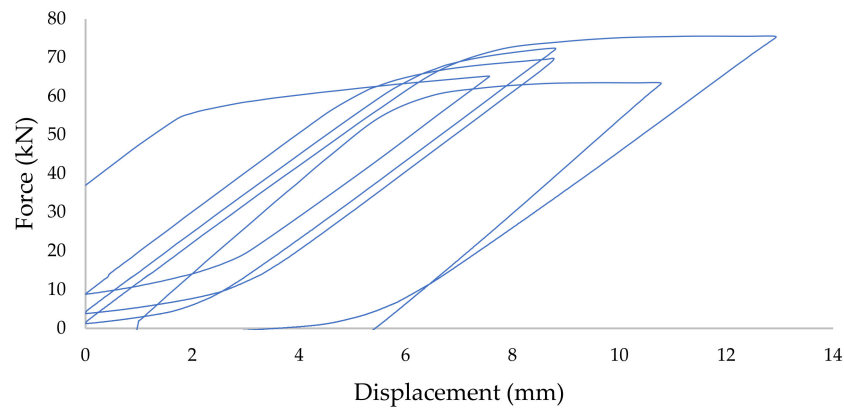
Figure 25. Numerical Force–Displacement with Interface Element for G40 concrete.

In contrast, UHPFRC with the interface element exhibited a force of up to 45.13 kN with a corresponding displacement of 10.7 mm (Figure 26), confirming the anticipated improvements in force and displacement accuracy as hypothesised.
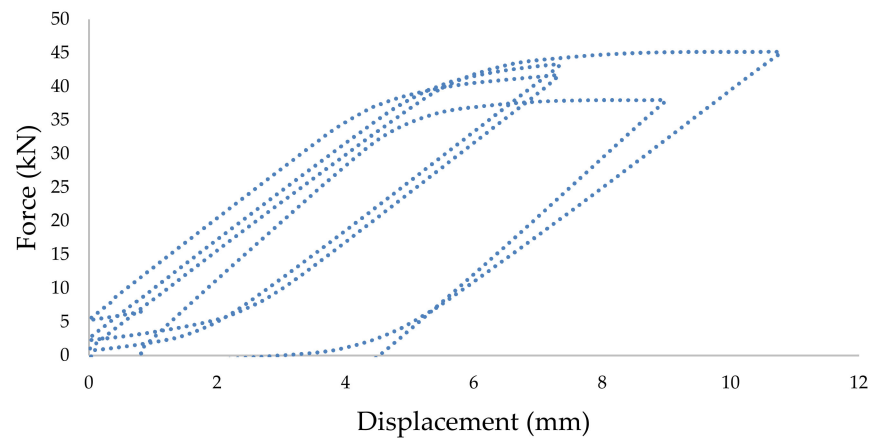
Figure 26. Numerical Force–Displacement with Interface Element for UHPFRC.

9. Discussion

The study aimed to enhance understanding of the relationship between Carbon-Fibre-Reinforced Polymer (CFRP) rods and both conventional Grade 40 concrete and Ultra-High-Performance Fibre-Reinforced Concrete (UHPFRC) under the demanding conditions of cyclic loading. Experimental and analytical findings revealed that the CFRP–UHPFRC bond exhibits significantly higher strength and displacement than the CFRP–concrete bond.

This remarkable performance stems from several factors: the superior tensile strength and stiffness of UHPFRC compared to concrete; the enhanced interfacial bonding between the CFRP rod and UHPFRC, attributable to the denser microstructure of UHPFRC; and the reduced cracking tendency of UHPFRC, resulting in more ductile bond behaviour.

Deliberate development and integration of an analytical interface element into a finite element model addressed the previously recognised gap in these models' ability to accurately replicate empirical data. The introduction of this interface element proved crucial, aligning computational predictions more closely with experimental results, thereby laying a foundation for the construction or rehabilitation of more reliable and robust infrastructure. The FEM model developed in this study demonstrated accurate predictions of load-bearing capacity, displacement at peak force, bond strength, and average shear stress along the CFRP rod for the CFRP–UHPFRC bond. Discrepancies between experimental and analytical results were within 10% for all parameters.

The enhanced Finite Element Method (FEM) centres around the incorporation of the interface element. Data presented in Table 15 highlight that initial simulations without the interface element exhibited significant deviations from experimental data. Notably, the maximum pull-out force was overestimated by a substantial 51.12%. The incorporation of the newly developed interface element effectively mitigated this difference, bringing the force prediction to a much-improved accuracy level of 8.38%. Additionally, the disparity in the critical parameter of displacement at peak forces was dramatically reduced from 12.89% without the interface element to an impressive 2.84% once the element was introduced into the model.

Table 15. Comparison of data.

Parameters		UHPFRC	Discrepancy	Improvement *
Maximum Pull-out Force (kN)	Numerical w/o Interface	70.00	51.12%	
	Experimental Data	41.50		42.74%
	Numerical with Interface	45.13	8.38%	
Displacement at Peak Force (mm)	Numerical w/o Interface	9.14	12.89%	
	Experimental Data	10.4		10.05%
	Numerical with Interface	10.7	2.84%	
Bond Strength (MPa)	Numerical w/o Interface	7.65	51.23%	
	Experimental Data	4.53		43.39%
	Numerical with Interface	4.9	7.84%	
Average Shear Stress along CFRP Rod (Pa)	Numerical w/o Interface	5.17	51.27%	
	Experimental Data	3.06		42.82%
	Numerical with Interface	3.33	8.45%	

* Improvement in accuracy of predictive simulations.

The efficacy of implementing the interface element is further emphasised by the improvement in bond strength predictions—a parameter of paramount importance for structural integrity where inaccuracies can lead to catastrophic miscalculations. The initial model projected bond strength at an overestimated figure that was 51.23% higher than the experimental observation. With the inclusion of the interface element, this figure was

corrected, with only 7.84% of error present, corresponding to a 43.39% improvement. This aspect of the model's improvement is particularly noteworthy, as bond strength directly influences the structural endurance and safety margins of built infrastructure.

The average shear stress along the CFRP rod is of utmost importance, and yet the original FEM significantly overestimated the stress by an astonishing 51.27%. With the incorporation of the interface element, the error was remarkably reduced to a negligible 8.45%, representing a significant advancement in precision.

The findings of this research underscore that interface elements are not mere computational artifacts but rather pivotal components, particularly for cyclic loading conditions. They hold the potential to transform finite element modelling from estimative guesswork into accurate, results-oriented predictive tools. Computational models equipped with these interface elements will provide critical insights into the future design, optimisation, and risk assessment protocols for concrete structures reinforced with CFRP rods.

The results of the study indicate that the combination of CFRP rods with UHPFRC offers superior performance compared to conventional Grade 40 concrete. This is attributed to the enhanced bonding strength and the ductile behaviour of UHPFRC, which can better accommodate the cyclic loading conditions (Figures 27 and 28).
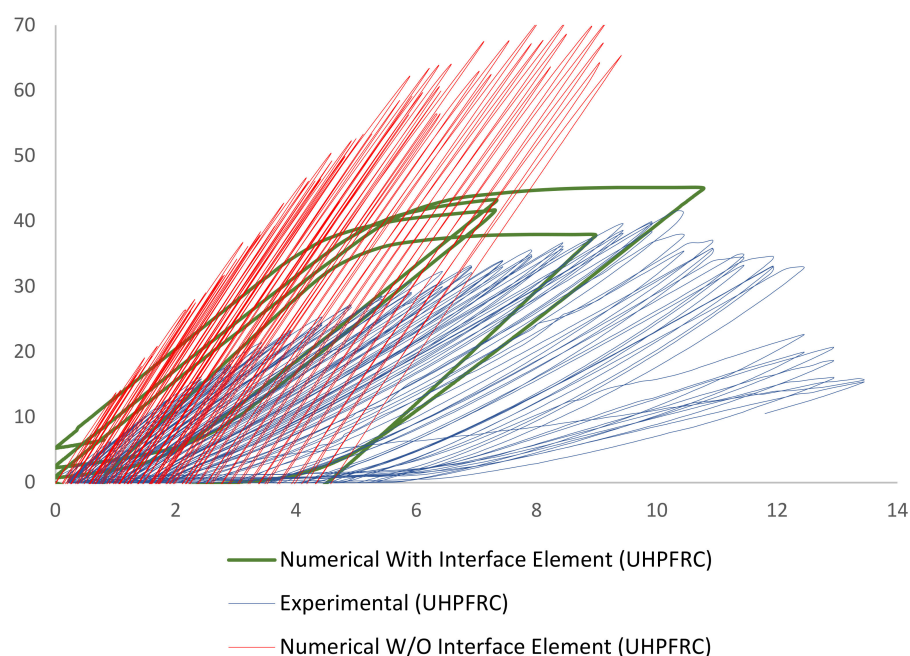
Figure 27. Force Comparison of UHPFRC.

The obtained results and comparisons of the interface elements demonstrate their efficacy, as they have been analytically formulated and validated based on experimental results. These results confirm that smooth CFRP has sufficient bonding properties to effectively reinforce concrete. However, when combined with high-performance concretes like UHPFRC, brittle CFRP exhibits exceptional performance due to the ductility of UHPFRC, which prevents abrupt damage to the CFRP composite. This is supported by the comparison presented in Table 16, which shows the data obtained by T Tibet Akbas et al. and the results of the current research [35].

T Tibet Akbas et al. investigated the behaviour of HSC specimens reinforced with ribbed CFRP rods under cyclic pull-out load testing. The comparison between the findings of the current research and Akbas et al.'s findings reveals a slight difference, with a roughly 50% discrepancy in carrying force. This discrepancy can likely be attributed to the type of CFRP bar utilised, as Akbas et al. [35] employed a ribbed CFRP bar, which enhances the bond between the CFRP rod and the cementitious material compared to the smooth CFRP bar used in the present study.
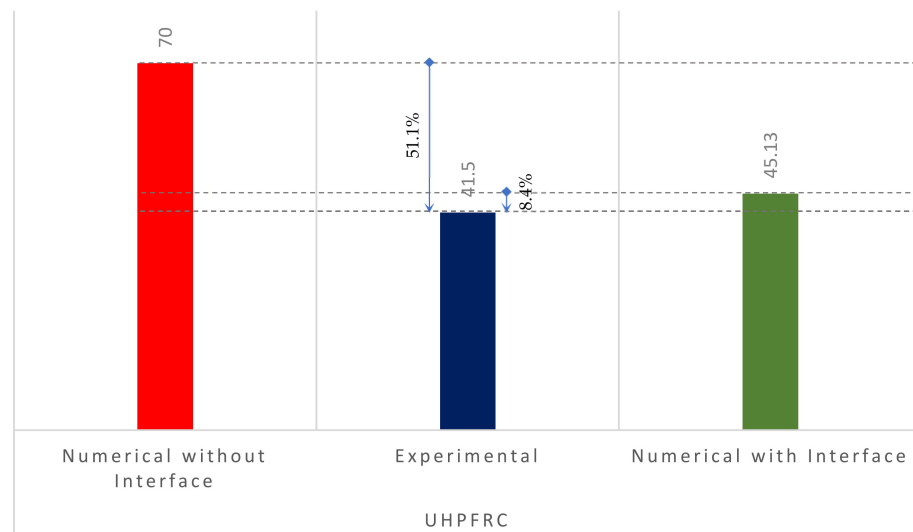
Figure 28. Force Discrepancy Comparison of UHPFRC.

Table 16. Result Comparison of T Tibet Akbas et al. With Current Research [35].

	Concrete	Type of CFRP	CFRP Bar Dia. (mm)	Length (mm)	Loading Type	Bond Stress (MPa)	Force (kN)	Failure Mode
T Tibet Akbas et al. [35]	HSC	Ribbed Bar	10	Min. 25D = 250	Cyclic	8.93	70.1	Concrete Splitting
Result of current Research	UHPFRC	Smooth Bar	9.7	Min. 25D ≈ 300	Cyclic	4.53	41.5	Rebar Rupture

Figure 29 compares the failure modes of Akbas et al.'s research and the current study's CFRP–UHPFRC specimens. However, the current study found a lower load carrying capacity. Despite this, CFRP bar rupture was the failure mode, which is a more favourable outcome than the concrete splitting observed in Akbas et al.'s study. This suggests that the combination of CFRP rods and UHPFRC provides a more favourable failure mode, contributing to the superior performance of this approach [35].
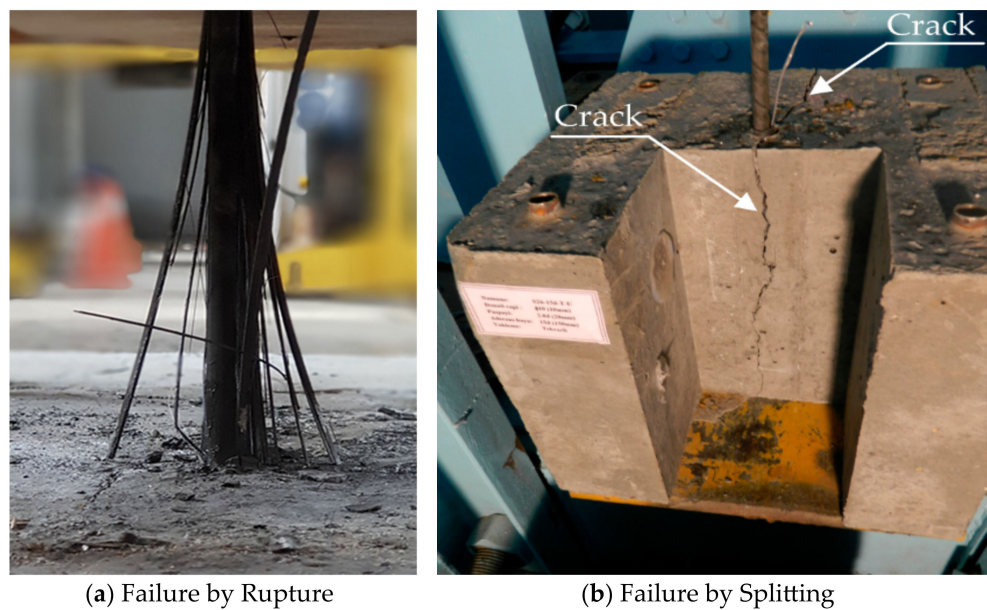

(**a**) Failure by Rupture

(**b**) Failure by Splitting

Figure 29. Failure mode: (**a**) Embedded CFRP Rod in UHPFRC; (**b**) Embedded CFRP Rod in HPC by T Tibet Akbas et al. [35].

10. Conclusions

This comprehensive study systematically examined the bonding performance of CFRP rods embedded in conventional concrete (Grade 40) and Ultra-High-Performance Fibre-Reinforced Concrete (UHPFRC) under cyclic loading conditions. The investigation delved into developing an analytical model to accurately predict the interaction between the embedded CFRP rods and the surrounding concrete matrix. Furthermore, the study aimed to elucidate the bonding characteristics of CFRP rods in concrete structures.

The key findings of this research yielded compelling insights:

1. CFRP rods exhibited exceptional bonding performance with UHPFRC, attributed to its superior ductility and strength capacity, particularly in tensile strength. This enhanced bonding significantly minimised cyclic-loading-induced fatigue failure, making UHPFRC–CFRP composites particularly suitable for applications involving heavy cyclic loading, such as parking lots, bridges, and other superstructures.

2. A substantial disparity emerged between the maximum pull-out forces of CFRP rods embedded in UHPFRC and G40 concrete. UHPFRC exhibited a remarkable 4-fold increase in pull-out force compared to G40 concrete. Additionally, UHPFRC demonstrated a significant delay in CFRP yielding time, approximately 650 increments more than G40 concrete.

3. Upon debonding between the CFRP rod and the concrete material, the force experienced a rapid drop followed by oscillations at a lower level, indicating that the CFRP rod retained its structural integrity despite the loss of bond.

4. The findings unequivocally demonstrated the exceptional bonding between UHPFRC and CFRP rods, a testament to the superior ductility of UHPFRC. In contrast, G40 concrete exhibited inferior bonding performance due to its brittle nature, which facilitated CFRP debonding from the concrete base prematurely, even before the CFRP rod reached its yielding point.

5. A comparison between the analytical interface element and the non-analytical interface element revealed a remarkable 10% improvement in displacement and a striking 42% improvement in pull-out force for UHPFRC when utilising the analytical interface element. This significant enhancement underscores the effectiveness of the analytical interface element when combined with UHPFRC.

6. The convergence of numerical and experimental results validated the accuracy of the research methodology and the reliability of the obtained findings. The comparison and analysis of the interface element further corroborated the efficacy of the analytical interface element, which was developed based on experimental data and analytical formulations. This interface element holds immense potential for more precise predictions of CFRP–UHPFRC bonding under cyclic loading conditions.

7. The study also affirmed the capability of smooth CFRP rods to effectively bond with concrete, particularly UHPFRC, which exhibits superior ductility and mitigates the risk of sudden CFRP damage.

In conclusion, this ground-breaking research has provided invaluable insights into the bonding performance of CFRP rods in conventional concrete and UHPFRC under cyclic loading. The findings demonstrate the exceptional bonding capabilities of UHPFRC–CFRP composites, making them a promising material for applications subjected to heavy cyclic loading. The developed analytical interface element has proven to be an invaluable tool for accurate predictions of CFRP–UHPFRC bonding behaviour, paving the way for enhanced design and optimisation of reinforced concrete structures incorporating CFRP reinforcement.

References

1. Bellis, M. The History of Concrete and Cement. Available online: http://theinventors.org/library/inventors/blconcrete.htm (accessed on 3 November 2021).
2. Quick Guide to the History of UHPC. Available online: https://www.uhpcsolutions.com/blog/quick-guide-to-the-history-of-uhpc (accessed on 8 January 2022).
3. Muzenski, S.; Graybeal, B. Structural Performance of UHPC Overlays. In Proceedings of the Third International Interactive Symposium on Ultra-High Performance Concrete, Wilmington, DE, USA, 4–7 June 2023.
4. You, X.; Lin, L.; Fu, B.; Xiang, Y. Ultra-high performance concrete reinforced with macro fibres recycled from waste GFRP composites. *Case Stud. Constr. Mater.* **2023**, *18*, e02120. [CrossRef]
5. Semendary, A.; Svecova, D. Numerical Simulation of the Load Transfer Mechanism at UHPC–UHPC Interface. In Proceedings of the Third International Interactive Symposium on Ultra-High Performance Concrete, Wilmington, DE, USA, 4–7 June 2023.
6. Ong, K.-Y.; Ma, C.-K.; Apandi, N.M.; Awang, A.Z.; Omar, W. Modeling of high-strength concrete-filled FRP tube columns under cyclic load. In *AIP Conference Proceedings: Proceedings of the 3rd International Conference on the Science and Engineering of Materials (ICoSEM 2017), Kuala Lumpur, Malaysia, 24–25 October 2017*; American Institute of Physics Inc.: College Park, MD, USA, 2018. [CrossRef]
7. Smith, S.; Teng, J. FRP-strengthened RC beams. I: Review of debonding strength models. *Eng. Struct.* **2002**, *24*, 385–395. [CrossRef]
8. Benmokrane, B.; Mohamed, H.; Ahmed, E. Recent developments of FRP bars as internal reinforcement in concrete structures & field applications. In Proceedings of the Fourth International Conference on Sustainable Construction Materials and Technologies, Las Vegas, NV, USA, 7–11 August 2016. [CrossRef]
9. Benmokrane, B.; Zhang, B.; Chennouf, A. Tensile properties and pullout behaviour of AFRP and CFRP rods for grouted anchor applications. *Constr. Build. Mater.* **2000**, *14*, 157–170. [CrossRef]
10. Zhao, J.; Li, X.; Zhang, X. Experimental and theoretical research on bond performance between CFRP bar and concrete under monotonic and reversed cyclic loading. *Eng. Struct.* **2021**, *246*, 112994. [CrossRef]
11. Cosenza, E.; Manfredi, G.; Realfonzo, R. Behavior and Modeling of Bond of FRP Rebars to Concrete. *J. Compos. Constr.* **1997**, *1*, 40–51. [CrossRef]
12. Zhou, H.; Fernando, D.; Nguyen, V.T.; Dai, J.-G. The bond behaviour of CFRP-to-concrete bonded joints under fatigue cyclic loading: An experimental study. *Constr. Build. Mater.* **2021**, *273*, 121674. [CrossRef]
13. Rashid, R.; Samsuddin, M.Z.; Riyad, A. Axial Strength of CFRP Strengthened Concrete Columns under Elevated Humid Environments. In Proceedings of the 12th International Symposium on Fiber Reinforced Polymers for Reinforced Concrete Structures (FRPRCS 12) & The 5th Asia-Pacific Conference on Fiber Reinforced Polymers in Structures (APFIS-2015), Nanjing, China, 14–16 December 2015.
14. American Concrete Institute. *Guide Test Methods for Fiber-Reinforced Polymers (FRPs) for Reinforcing or Strengthening Concrete Structures*; Reported by ACI Committee 440; American Concrete Institute: Farmington Hills, MI, USA, 2004.
15. Alkhrdaji, T.; Fyfe, E.R.; Korff, J.; Schupack, M.; Bakis, C.E.; Gentry, T.R.; Shield, C.K. Guide for the Design and Construction of Structural Concrete Reinforced with FRP Bars. 2006. Available online: http://biskagroup.com/wp-content/uploads/2018/07/440.1R-06-Guide-for-the-Design-and-Construction-of-Structural-Concrete-Reinforced-with-FRP-Bars.pdf (accessed on 10 October 2021).
16. Akbas, T.T.; Celik, O.C.; Yalcin, C. Experimental bond behaviour of deformed CFRP rebars in high strength concrete. In Proceedings of the Concrete—Innovation and Design: FIB Symposium Proceedings, Copenhagen, Denmark, 18–20 May 2015; pp. 283–284.
17. *BS 5328 Part 2*; Concrete Part 2: Methods for Specifying Concrete Mixes. British Standards Institution: Nottingham, UK, 2002.
18. *ASTM 820*; Standard Specification for Steel Fibers for Fiber-Reinforced Concrete ASTM820/ASTM820M-11. ASTM International: West Conshohocken, PA, USA, 2006.
19. *BS EN14889*; Ophthalmic Optics. Spectacle Lenses. Fundamental Requirements for Uncut Finished Lenses. British Standards Institution: London, UK, 2013.
20. Habel, K.; Viviani, M.; Denarié, E.; Brühwiler, E. Development of the mechanical properties of an Ultra-High Performance Fiber Reinforced Concrete (UHPFRC). *Cem. Concr. Res.* **2006**, *36*, 1362–1370. [CrossRef]
21. Le Hoang, A.; Fehling, E. Influence of steel fiber content and aspect ratio on the uniaxial tensile and compressive behavior of ultra high performance concrete. *Constr. Build. Mater.* **2017**, *153*, 790–806. [CrossRef]

22. Hafezolghorani, M.; Hejazi, F.; Vaghei, R.; bin Jaafar, M.S.; Karimzade, K. Simplified damage plasticity model for concrete. *Struct. Eng. Int.* **2017**, *27*, 68–78. [CrossRef]

23. Applied Technology Council. *Guidelines for Cyclic Seismic Testing of Components of Steel Structures for Buildings*; Report No. ATC-24; Applied Technology Council: Redwood City, CA, USA, 1992.

24. Uomoto, T.; Ishibashi, T.; Nobuta, Y.; Satoh, T.; Kawano, H.; Takewaka, K.; Uji, K. Standard Specifications for Concrete Structures-2007 by Japan Society of Civil Engineers. *Concr. J.* **2008**, *46*, 3–14. [CrossRef] [PubMed]

25. RILEM, T.C. *RILEM Recommendations for the Testing and Use of Constructions Materials*; CRC Press: London, UK, 1994.

26. *BS EN 12390: 2002*; Testing Hardened Concrete. Part 3, Compressive Strength of Test Specimens. BSI: London, UK, 2002.

27. British Standards Institution. Testing Hardened Concrete. In *Part 3, Compressive Strength of Test Specimens*; British Standards Institution: London, UK, 2002.

28. Hamad, A.J. Size and shape effect of specimen on the compressive strength of HPLWFC reinforced with glass fibres. *J. King Saud Univ. Eng. Sci.* **2017**, *29*, 373–380. [CrossRef]

29. Yu, R.; Spiesz, P.; Brouwers, H.J.H. Mix design and properties assessment of Ultra-High Performance Fibre Reinforced Concrete (UHPFRC). *Cem. Concr. Res.* **2014**, *56*, 29–39. [CrossRef]

30. Yao, L.-Z.; Wu, G. Nonlinear 2D Finite-Element Modeling of RC Beams Strengthened with Prestressed NSM CFRP Reinforcement. *J. Compos. Constr.* **2016**, *20*, 04016008. [CrossRef]

31. Esfahani, M.H.; Hejazi, F.; Vaghei, R.; Nikbakht, E.; Tze, D.C.J. Development of Constitutive Model for Precast Prestressed Concrete Segmental Columns. *Model. Simul. Eng.* **2016**, *2016*, 9453649. [CrossRef]

32. Deobald, L.; Mabson, G.; Dopker, B.; Hoyt, D.; Baylor, J.; Graesser, D. Interlaminar fatigue elements for crack growth based on virtual crack closure technique. In Proceedings of the Collection of Technical Papers—AIAA/ASME/ASCE/AHS/ASC Structures, Structural Dynamics and Materials Conference, Honolulu, HI, USA, 23–26 April 2007; Volume 5, pp. 4656–4663. [CrossRef]

33. Qian, Q.; Xie, D. Analysis of mixed-mode dynamic crack propagation by interface element based on virtual crack closure technique. *Eng. Fract. Mech.* **2007**, *74*, 807–814. [CrossRef]

34. Luis, F.; Moncayo, G. *Numerical Modelling of Failure in Advanced Composite Materials*; Woodhead Publishing: Sawston, UK, 2015.

35. Akbas, T.T.; Celik, O.C.; Yalcin, C.; Ilki, A. Monotonic and cyclic bond behavior of deformed CFRP bars in high strength concrete. *Polymers* **2016**, *8*, 211. [CrossRef] [PubMed]